

CATHARINE DE VITA GRAVES

Automatic quantification of cardiac left ventricle deformation in  
magnetic resonance images

São Paulo

2023

ESCOLA POLITÉCNICA DA UNIVERSIDADE DE SÃO PAULO

CATHARINE DE VITA GRAVES

Automatic quantification of cardiac left ventricle deformation in  
magnetic resonance images

Versão corrigida

Thesis presented to the Escola Politécnica  
da Universidade de São Paulo to obtain  
the degree of Doctor of Science.

Area of concentration: Biomedical  
Engineering

Supervisor: Marco Antonio Gutierrez


São Paulo

2023

Autorizo a reprodução e divulgação total ou parcial deste trabalho, por qualquer meio convencional ou eletrônico, para fins de estudo e pesquisa, desde que citada a fonte.

Este exemplar foi revisado e corrigido em relação à versão original, sob responsabilidade única do autor e com a anuência de seu orientador.

São Paulo, 19 de outubro de 2023

Assinatura do autor: 

Assinatura do orientador: Marco Antonio Gutierrez

Assinado de forma digital por  
Marco Antonio Gutierrez  
Dados: 2023.10.19 12:09:58 -03'00'

#### Catálogo-na-publicação

Graves, Catharine De Vita  
Automatic quantification of cardiac left ventricle deformation in magnetic resonance images / C. D. V. Graves -- versão corr. -- São Paulo, 2023.  
106 p.

Tese (Doutorado) - Escola Politécnica da Universidade de São Paulo.  
Departamento de Engenharia de Telecomunicações e Controle.

1.Myocardium deformation 2.Cardiac motion 3.Deep learning  
I.Universidade de São Paulo. Escola Politécnica. Departamento de Engenharia de Telecomunicações e Controle II.t.

*Aos verdadeiros financiadores desta pesquisa, a classe trabalhadora brasileira.*

## ACKNOWLEDGMENTS

I would like to express my deepest gratitude to my family for their support and encouragement throughout my academic journey. Their love and sacrifices have been a constant source of motivation for me.

I would also like to thank my close friends for their support, encouragement, and understanding during the ups and downs of the doctoral journey. Your unwavering belief in me and willingness to listen, advise, and cheer me up has been invaluable.

I extend my appreciation to my coworkers for their valuable assistance, stimulating discussions, and productive collaboration. Their support has made my work more enjoyable and rewarding.

I would like to express my sincerest appreciation to my advisor for his guidance, wisdom, and encouragement. Your constant support, mentorship, and constructive feedback have been a great source of inspiration and motivation.

Lastly, I would like to express my deep gratitude to the Brazilian inclusion public programs for their support during my undergraduate studies. Without their support, achieving a PhD level of study would have been almost impossible. Their commitment to provide access and opportunities to students from diverse backgrounds has allowed me to pursue my academic and research goals.

## ABSTRACT

Systems designed to prevent or aid in the diagnosis of cardiovascular diseases can greatly reduce mortality rates associated with these diseases, which are the leading global causes of death. The precise measurement of cardiac parameters provides essential data for diagnosing cardiomyopathies and evaluating the effectiveness of treatments. Cardiomyopathies can be assessed using cardiac magnetic resonance images (CMR), considered the gold standard imaging technique for evaluating cardiac function and deformation (strain). Myocardial strain measurement offers additional insights for predicting a patient's prognosis. Nevertheless, quantifying strain in CMR images is a challenging task, and numerous inter- and intra-modality discrepancies hinder its adoption in clinical practice. The most popular methods for determining myocardial strain typically involve manual or semi-automated segmentation, followed by motion tracking. Even when performed by a qualified expert, myocardium segmentation is time-consuming and costly. Furthermore, in CMR images, the highly uniform brightness intensity within the myocardium makes it difficult to accurately segment the cardiac walls, which limits currently available motion-tracking methods. A subcategory of machine learning, known as deep learning (DL) has shown substantial promise in various medical applications. As it does not depend on human interaction and subjectivity, the application of DL approaches has the potential to improve the accuracy of myocardial parameter quantification, including myocardium deformation, with potentially reduced variability. Since the trained DL model is deterministic, the findings from successive analyses of the same image are consistent. In this study, we introduced and evaluated a novel DL-method for quantifying myocardial strain in CMR images with 2D-SSFP pulse sequence. We developed a hybrid pipeline that combines supervised and unsupervised DL approaches to automate tasks related to cardiac muscle segmentation and motion estimation. We explored the generalizability of a supervised DL segmentation method for delineating the cardiac muscle and employed an unsupervised DL model to track motion in the left ventricle in both real and synthetic 3D cine magnetic resonance images. Finally, we investigated the relationship between the segmented myocardium and the estimated motion to quantify myocardial strain. The results of this study highlight the potential of DL-based approaches to automate and improve the accuracy of myocardial strain quantification. Our proposed hybrid pipeline exhibited promising

results in accurately segmenting the cardiac muscle and tracking its motion, which can aid in the diagnosis and monitoring of cardiac diseases, reduce the need for manual intervention, and save time. In summary, this work underscores the potential of DL in enhancing the precision and efficiency of cardiac imaging analysis.

**Keywords:** Myocardium deformation; Cardiac motion; Deep learning.

## RESUMO

Sistemas que possibilitam a prevenção ou auxílio no diagnóstico de doenças cardiovasculares podem contribuir para a redução da mortalidade por essas condições, que são as principais causas de morte no mundo. A quantificação precisa dos parâmetros cardíacos permite o acesso a dados fundamentais para o diagnóstico de cardiomiopatias e também possibilita a avaliação da eficácia dos tratamentos. As cardiomiopatias podem ser avaliadas utilizando imagens de ressonância magnética cardíaca (RMC), que é considerada a técnica de imagem padrão-ouro para acessar a função cardíaca e a deformação (*strain*) cardíaca. A deformação do miocárdio fornece informações adicionais para prever prognóstico de um paciente. No entanto, quantificar a deformação em imagens de RMC é uma tarefa desafiadora, e inúmeras discrepâncias inter e intra-modalidade dificultam sua adoção na prática clínica. Os métodos mais populares para determinar a deformação do miocárdio geralmente envolvem a segmentação manual ou semi-automatizada, seguida pelo rastreamento de movimento. Mesmo quando realizada por um especialista qualificado, a segmentação do miocárdio é um processo demorado e custoso para ser concluído. Além disso, nas imagens de RMC cardíaca, a intensidade uniforme de brilho altamente no interior do miocárdio dificulta a segmentação correta das paredes cardíacas, o que limita os métodos de rastreamento de movimento disponíveis atualmente. Um subconjunto das técnicas de aprendizado de máquina, conhecido como aprendizado profundo (AP), demonstrou um potencial considerável em uma variedade de aplicações médicas. Como não depende da interação e subjetividade humana, a aplicação de abordagens AP pode melhorar o desempenho da quantificação de parâmetros do miocárdio, como a deformação, com possivelmente redução da variabilidade. Como o modelo de AP treinado é determinístico, os resultados de análises sucessivas da mesma imagem são consistentes. Neste trabalho, propusemos e avaliamos um novo método baseado em AP para quantificar a deformação miocárdica em RMC com sequência de pulso do tipo 2D-SSFP. Desenvolvemos uma sequência híbrida que utiliza AP supervisionado e não-supervisionado para automatizar as tarefas envolvidas na segmentação do músculo cardíaco e na estimativa do seu movimento. Investigamos a generalizabilidade de um método de segmentação de AP supervisionado para delinear o músculo cardíaco e usamos um modelo de AP não supervisionado para rastrear o



movimento no ventrículo esquerdo em imagens de ressonância magnética cinética 3D reais e sintéticas. Por fim, investigamos a relação entre o miocárdio segmentado e o movimento estimado no músculo para quantificar a deformação do miocárdio. Os resultados deste estudo demonstram o potencial das abordagens baseadas em AP para automatizar e melhorar a precisão da quantificação da deformação miocárdica. A sequência proposta mostrou resultados promissores na segmentação precisa do músculo cardíaco e no rastreamento do seu movimento, o que pode auxiliar no diagnóstico e monitoramento de doenças cardíacas, reduzir a necessidade de intervenção manual e economizar tempo. Em geral, este trabalho destaca o potencial do AP em melhorar a precisão e eficiência da análise de imagens cardíacas.

Palavras-chave: Deformação do miocárdio; movimento cardíaco; aprendizado profundo.

# CONTENTS

<b>LIST OF FIGURES</b> .....	12
<b>LIST OF TABLES</b> .....	17
<b>LIST OF ABBREVIATIONS</b> .....	18
<b>LIST OF SYMBOLS</b> .....	20
<b>1. INTRODUCTION</b> .....	22
<b>1.1. Objectives</b> .....	27
<b>2. BACKGROUND</b> .....	28
<b>2.1. Magnetic resonance image</b> .....	28
<b>2.2. Cardiac anatomy</b> .....	30
<b>2.3. Deep learning</b> .....	31
<b>2.4. Myocardium segmentation</b> .....	36
<b>2.5. Cardiac movement in CMR images</b> .....	37
<b>2.6. Cardiac strain</b> .....	38
<b>2.7. Parameters visualization</b> .....	42
<b>3. LITERATURE REVIEW</b> .....	44
<b>3.1. CNN generalization in myocardium segmentation</b> .....	44
<b>3.2. CNN to quantify cardiac movement in CMR images</b> .....	48
<b>3.3. Automatic pipeline to estimate strain with CNN-based motion quantification</b> .....	50
<b>4. METHODOLOGY</b> .....	51
<b>4.1. Myocardium segmentation</b> .....	52
<b>4.2. Motion quantification</b> .....	60
<b>4.3. Strain</b> .....	65
<b>5. RESULTS AND DISCUSSION</b> .....	69
<b>5.1. Myocardium segmentation</b> .....	69

<b>5.2. Motion quantification</b> .....	72
<b>5.3. Strain</b> .....	76
<b>6. CONCLUSION</b> .....	92
<b>7. PUBLISHED ARTICLES</b> .....	93
<b>8. BIBLIOGRAPHY</b> .....	95

## LIST OF FIGURES

Figure 1: Positioning of the long-axis and short-axis acquisition in the heart (a), an example of a long-axis image (b), and a short-axis image (c).....	23
Figure 2: CMR images in different phases, highlighting the myocardium inside the green hollow circle: (a) diastole, when the myocardium is relaxed; and (b) systole when the myocardium is contracted.....	23
Figure 3: CMR short-axis image without segmentation (a) indicating the right ventricle (RV) and the left ventricle (LV); and with segmentation (b) of the epicardium, endocardium, and papillary muscles. ....	25
Figure 4: Different myocardium inner boundary (endocardium) segmentation (right) affecting the estimated global longitudinal strain (GLS) (left) (AMZULESCU, DE CRAENE, <i>et al.</i> , 2019).....	25
Figure 5: Proposed hybrid pipeline, which includes supervised (Myocardium segmentation) and unsupervised DL modules, and an analytical module (Strain quantification).....	27
Figure 6: Protons have parallel (low energy) or antiparallel (high energy) states related to the external magnetic field (B). The population of protons in a high-energy state increases (longitudinal magnetization decreases) when a RF pulse is irradiated and the protons begin to precess in phase (increase in transverse magnetization). The protons return to their original condition when the RF pulse is turned off. Longitudinal magnetization recovers (adapted from DARTON, IONESCU, <i>et al.</i> , 2019).....	29
Figure 7: scheme of the heart structure (WAPCAPLET, 2003).....	30
Figure 8: Relationship between different AI techniques and an example of each technique. ....	32
Figure 9: MLP architecture example, with two hiding layers (adapted from HAYKIN, 2008).....	33

Figure 10: Example of 2D convolution operation as used in neural network. The operation performed in this example reduces the input size (GOODFELLOW, BENGIO, <i>et al.</i> , 2016).....	34
Figure 11: Example of max-pooling operation with a 2x2 window.....	35
Figure 12: Simple scheme of a CNN composed of convolutions, pooling, and fully connected layers (CHEN, QIN, <i>et al.</i> , 2020).....	36
Figure 13: Variation among CMR images. ....	37
Figure 14: Basic concept of feature tracking in CMR images. This technique consists of determining small squares in the first image (left) and then looking for the possible displacement of the gray pattern in the next image (right) (PEDRIZZETTI, CLAUS, <i>et al.</i> , 2016).....	38
Figure 15: Different ways to calculate strain: Lagrangian (left) and Eulerian (center); And the difference in the strain curve along the cardiac cycle depending on the calculation used (right) (AMZULESCU, DE CRAENE, <i>et al.</i> , 2019).....	40
Figure 16: Illustration of longitudinal ( <i>L</i> ), radial ( <i>R</i> ), and circumferential ( <i>C</i> ) components in a point in the left ventricle surface. ....	42
Figure 17: Diagram of standardized LV segments definition proposed by AHA and its respective nomenclature, indicating the anatomical position of the segment (CERQUEIRA, WEISSMAN, <i>et al.</i> , 2002).....	43
Figure 18: Polar plot used to standardize the displaying of cardiac information by AHA, showing the position of the 17 myocardial segments and its nomenclature (CERQUEIRA, WEISSMAN, <i>et al.</i> , 2002).....	44
Figure 19: Strain quantification process using two input volumes of stacked CMR images at time 0 ( $t_0$ ) and time n ( $t_n$ ). With (A) the LiteResnet used to segment the myocardium and (B) the PWC Siamese network to compute the motion field from $t_0$ to $t_n$ ( $\phi_0$ ) and from $t_n$ to $t_0$ ( $\phi_n$ ), creating the average motion field ( $\phi$ ) used to determine the strain in the myocardium (C).....	52
Figure 20: LiteResnet architecture used to segment the myocardium in CMR images.	53
Figure 21: Scheme of the residual block used in the backbone of the Lite ResUnet. ....	53

Figure 22: PWC network used as the main component of the Siamese network. Inputs are composed of two volumes acquired at consecutive frames ( $t_0$ and $t_n$ ); Then, the images go through a series of dimensionality reduction (Downsampling) and feature extraction and warp transformation blocks, cost volume, and optical flow estimator.....	61
Figure 23: Siamese network architecture. ....	62
Figure 24: (A) Example of short axis cardiac image generated by the XCAT and (B) the same image transformed into a CMR pattern using MRXCAT. ....	63
Figure 25: Example of 5 concentric contours division (right) performed in the myocardium area. ....	65
Figure 26: Illustration of the wall motion score classes: normal, hypokinetic, akinetic, and dyskinetic (LEISCHIK, DWORRAK, <i>ET AL.</i> , 2016). ....	67
Figure 27: Average Dice score during training process of the U-net (left) and LiteResNet (right) for the training set and validation set. ....	69
Figure 28: Example of the difference between the ground truth myocardium mask in the Sunnybrook (left) and the segmented by the model trained with the ACDC data (right). ....	71
Figure 29: Example of displacement field obtained from a health simulated subject in the Xcat. All the figures on the left are constructed with data simulated by the Xcat and on the left generated by the PWC Siamese network, in the columns, there are the displacements in the x direction, y direction, and z direction, along with the respective color code representing the amount of movement in that direction. The displacement field outside the myocardium mask was set to zero to ease the visualization. ....	75
Figure 30: Radial strain calculated with the displacement field learned by the PWC Siamese network for a normal case (left) and a patient with myocardial infarction (right). ....	77
Figure 31: Circumferential strain calculated with the displacement field learned by the PWC Siamese network for a normal case (left) and a patient with myocardial infarction (right). ....	77

Figure 32: Longitudinal strain calculated with the displacement field learned by the PWC Siamese network for a normal case (left) and a patient with myocardial infarction (right). .....	78
Figure 33: Comparison of the variation of healthy global systolic radial strain obtained by the PWC Siamese method, the Medis and CVI 42, with some values reported in the literature.....	79
Figure 34: Comparison of the variation of healthy global systolic circumferential strain obtained by the PWC Siamese method, the Medis and CVI 42, with some values reported in the literature.....	79
Figure 35: Box-plot of the global radial strain (GRS) calculated using the motion field from de ground truth XCAT and from the PWC Siamese, the B-Spline registration and the optical flow. Exams are divided into three ejection fraction categories: normal (N), lower function (LF) and heart failure (HF). ....	81
Figure 36: Box-plot of the global circumferential strain (GCS) calculated using the motion field from de ground truth XCAT and from the PWC Siamese, the B-Spline registration and the optical flow. Exams are divided into three ejection fraction categories: normal (N), lower function (LF) and heart failure (HF).....	81
Figure 37 Box-plot of the global longitudinal strain (GLS) calculated using the motion field from de ground truth XCAT and from the PWC Siamese, the B-Spline registration and the optical flow. Exams are divided into three ejection fraction categories: normal (N), lower function (LF) and heart failure (HF).....	82
Figure 38: Box plot comparing WMS class distribution with strain values obtained by the CVI 42, Medis, and strain quantification using the PWC Siamese networks (our method), optical flow and Bspline displacement fields. ....	83
Figure 39: (up) Global radial strain (GRS) and (bottom) global circumferential strain (GCS) for all the strain quantification methods Medis, CVI, our method, optical flow and Bspline for each group of subjects: normal (NOR) and not normal (NOT NOR). ....	84
Figure 40: ROC curve for the classification system using logistic regression to classify normal and not normal WMS classes using radial strain data from our method, CVI 42	

system, Medis system, optical flow and bspline method, using 4-folds cross-validation. .....	85
Figure 41: ROC curve for the classification system using logistic regression to classify normal and not normal WMS classes using circumferential strain data from our method, CVI 42 system, Medis system, optical flow and bspline method, using 4-folds cross-validation. ....	86
Figure 42: Bland-Altman plot for the intra-observer radial local strain in the CVI 42 system (orange) and Medis System (green). ....	87
Figure 43: Bland-Altman plot for the intra-observer circumferential local strain in the CVI 42 system (orange) and Medis System (green).....	88
Figure 44: Bland-Altman plot for the inter-observer analysis with radial local strain, performed with the Medis (green) and CVI 42 (orange) data. ....	88
Figure 45: Bland-Altman plot for the inter-observer analysis with circumferential local strain, performed with the Medis (green) and CVI 42 (orange) data. ....	89
Figure 46: Global radial strain over the cardiac cycle resulted by the application of our pipeline (left) and the DeepStrain (right) in the M&Ms-2 dataset, showing the curves for the normal group (NOR) and not normal (NOT NOR).....	91



## LIST OF TABLES

Table 1: Datasets details .....	57
Table 2: Endocardium Dice scores obtained with U-net and LiteResnet tested in set samples from the datasets ACDC, INC, SUN, LVSC, and M&Ms-2.....	70
Table 3: Epicardium Dice scores obtained with U-net and LiteResnet tested in set samples from the datasets ACDC, INC, SUN, LVSC, and M&Ms-2.....	70
Table 4: Myocardium Dice scores obtained with U-net and LiteResnet tested in set samples from the datasets ACDC, INC, SUN, LVSC, and M&Ms-2.....	70
Table 5: Dice obtained comparing the fixed myocardium mask and the warped moving myocardium mask using the displacement field generated by different methods (Optical flow, B-spline registration, PWC network, PWC Siamese network and reported in the literature – Carmen) for the ACDC, INC, and Xcat datasets. ....	73
Table 6: Mean absolute error (MAE), end-point-error (EPE), and percentage of correct pixel (PCP) between the Xcat displacement field and the generated by optical flow technique, B-spline registration, PWC network, PWC Siamese network and reported in the literature (Carmen).....	74
Table 7: Mean absolute error between the calculated strain using the Xcat displacement field and the generated by Optical Flow, B-Spline registration, PWC network, and PWC Siamese network, for each strain direction: radial, circumferential and longitudinal....	80
Table 8: MAE for the CVI 42 and Medis intra- and inter-observer analyses. ....	87
Table 9: Number of trainable parameters and average inference time of the models, including the segmentation models and the motion estimation models.....	92

## LIST OF ABBREVIATIONS

ACDC	Automated Cardiac Diagnosis challenge
ADAM	Adaptive Moment Estimation
AHA	American Heart Association
AI	Artificial Intelligence
AUC	Area Under the Curve
BCE	Binary Cross-Entropy
CI	Confidence Interval
CLAHE	Contrast Limited Adaptive Histogram Equalization
CMR	Cardiac Magnetic Resonance
CNN	Convolutional neural network
DL	Deep Learning
ED	End Diastole
EF	Ejection Fraction
EPE	End Point Error
ES	End Systole
FID	Free Induction Decay
GCS	Global Circumferential Strain
GLS	Global Longitudinal Strain
GRS	Global Radial Strain
HD	Hausdorff distance
HF	Heart Failure
HYP	hypertrophy
INC	Instituto do Coração – HCFMUSP
LF	Lower Function
LV	Left Ventricle
LVSC	Left Ventricle Segmentation Challenge
MAE	Mean Absolute Error
MICCAI	The Medical Image Computing and Computer-Assisted Intervention Society
MLP	Multilayer Perceptron
MRI	Magnetic Resonance Imaging
MRXCAT	Magnetic Resonance Extended Cardiac-Torso
OF	Optical Flow
PCP	Percentage of Correct Pixel
PWC	Pyramid, Warping, and Cost Volume
RF	Radiofrequency
ROC	Receiver Operating Characteristic
ROI	Region of Interest
RV	Right Ventricle

SSFP	Steady-State Free Precession
STACOM	Statistical Atlases and Computational Modeling of the Heart
SUN	Sunnybrook Health Sciences Centre
WMS	Wall Motion Score
XCAT	Extended Cardiac-Torso

## LIST OF SYMBOLS

$\omega$	Larmor frequency
$\gamma$	Gyromagnetic ratio
$B$	Magnetic field
$y_k$	Artificial neuron output at position $k$
$w_k$	Synaptic weights at the position $k$
$b_k$	Bias at the position $k$
$\varphi(\bullet)$	Activation function
$K$	Kernel
$I$	Image input
$\varepsilon$	Cardiac deformation or strain
$L$	Length
$L_0$	Initial length
$L(t)$	Length at time instant $t$
$t_0$	Time instant initial
$t_n$	Time instant $n$
$dt$	An infinitesimal interval of time
$d\varepsilon$	The infinitesimal interval of strain
$F$	Gradient tensor
$\phi$	Displacement vector field
$\hat{\phi}$	Learned displacement vector field
$x, y, \text{ and } z$	Displacement in Cartesian directions
$E_C$	Strain tensor in Cartesian
$\hat{L}$	Longitudinal direction
$\hat{C}$	Circumferential direction
$\hat{R}$	Radial direction
$\Theta$	Rotation matrix
$V$	Volume
$V_w$	Warped volume
$\mu$	Average intensity
$\alpha, c_1 \text{ and } c_2$	Constants
$\sigma$	Variance

$\sigma_{VVW}$	covariance of V and $V_W$
$\Omega$	Domain of $\hat{\phi}$
u, v, and w	Components of the displacement vector in x, y, and z

## 1. INTRODUCTION

Cardiovascular diseases stand as the leading cause of global mortality, as reported by the World Health Organization. In 2019, approximately 17.9 million people died of complications related to cardiovascular diseases, with 85% of these deaths attributed to heart attacks or strokes (WORLD HEALTH ORGANIZATION, 2021).

Among the various medical imaging techniques available for assessing cardiac function, cardiac magnetic resonance (CMR) is considered the gold standard for diagnosing cardiomyopathies (EPSTEIN, 2007), as it presents a better signal-to-noise ratio and does not use ionizing radiation as in Nuclear Medicine and Tomography (KRAMER, 2015, PATEL, KRAMER, 2017). The CMR allows the quantification of cardiac structures, such as the left ventricle (LV) and right ventricle (RV) over the cardiac cycle. Accurate quantification of these structures is important to estimate physiological parameters, such as chamber size and ejection fraction. To assess physiological parameters associated with the LV, the commonly employed acquisition sequence is the 2D cine steady-state free precession (2D-SSFP Cine MR), with acquisition performed in the cardiac long axis and a stack of the short axis along the cardiac cycle. Figure 1a shows the cardiac orientation during the long and short-axis acquisition, with an example of a long-axis image (1b) and a short-axis image (1c).



Figure 1: Positioning of the long-axis and short-axis acquisition in the heart (a), an example of a long-axis image (b), and a short-axis image (c).

Normally a CMR exam is composed of a sequence of images acquired over the cardiac cycle. Figure 2 shows two images in different phases, diastole (when the myocardium is relaxed) and systole (when the myocardium contracts).

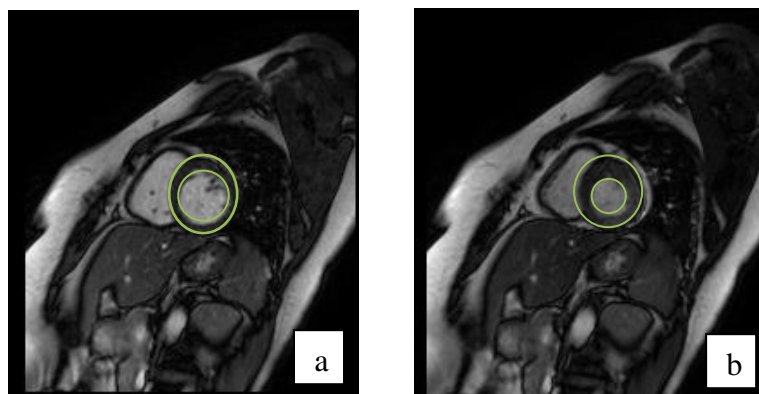


Figure 2: CMR images in different phases, highlighting the myocardium inside the green hollow circle: (a) diastole, when the myocardium is relaxed; and (b) systole when the myocardium is contracted.

Accurate quantification of global and local parameters allows to access vital information to diagnose cardiomyopathies, combined with valuable data to evaluate treatment effectiveness. Global parameters, such as ejection fraction (EF), systolic

volume, and myocardial thickness, play a crucial role in the comprehensive evaluation of cardiac function. On the other hand, local parameters, such as motion, deformation, or strain provide localized information within the cardiac muscle, allowing the characterization of local lesions and their extent. Consequently, the precise determination of these parameters is essential to cardiovascular disease diagnosis and progression monitoring (HUI WANG, AMINI, 2012).

The most common methods to quantify global and local parameters typically begin with manual or semi-automated segmentation, and in some cases followed by a motion tracking techniques, such as feature tracking or image registration (AMZULESCU, DE CRAENE, *et al.*, 2019). However, segmentation is not trivial, and a time-consuming task, even if performed by a skilled professional. CMR can present challenges due to low contrast between the myocardium and surrounding tissues, variation of intensity among acquisitions, and, complex structures variation among patients, moreover, there is a lack of consensus about including or not the papillary muscles (BERNARD, LALANDE, *et al.*, 2018, COLLETTI, 2019, SUINESIAPUTRA, COWAN, *et al.*, 2014). These sources of image disparity impact the delineation of the myocardium boundaries, the epicardium, and the endocardium. A study (BHUVA, BAI, *et al.*, 2019) showed that there is an inter- and intra-observer variation of the myocardium segmentation, which can significantly impact the quantification of the cardiac parameters. Figure 3 shows a short axis CMR image without the segmentation (a) and with the segmentation of the epicardium, endocardium, and papillary muscles (b). It can be observed in Figure 3 the regions in the myocardium boundaries with low contrast difference between the surrounding tissues.



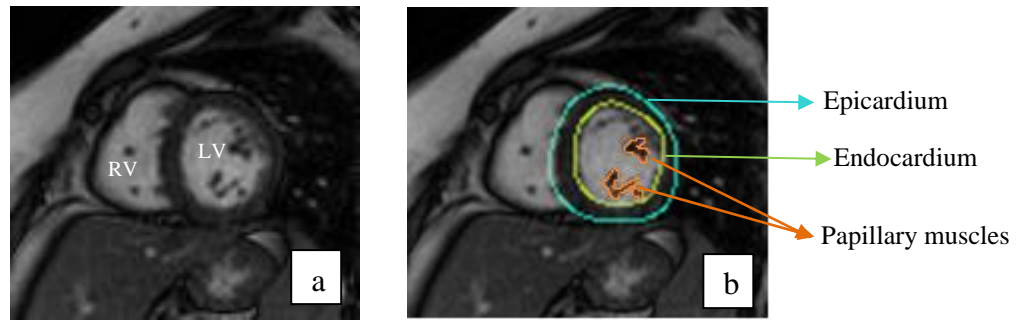


Figure 3: CMR short-axis image without segmentation (a) indicating the right ventricle (RV) and the left ventricle (LV); and with segmentation (b) of the epicardium, endocardium, and papillary muscles.

Some parameters, especially the most used global parameters (such as ejection fraction, myocardium mass, and cavity volume) can be directly derived after the segmentation of the cardiac structure of interest. However, the quantification of most local parameters needs the use of additional methods after the segmentation of the LV to quantify the muscle movement. Delineation of the LV boundaries can significantly affect the estimation of the global and local parameters. Figure 4 shows an example of the different segmentation impacts on the resulting global longitudinal strain (GLS) over the cardiac cycle (AMZULESCU, DE CRAENE, *et al.*, 2019).

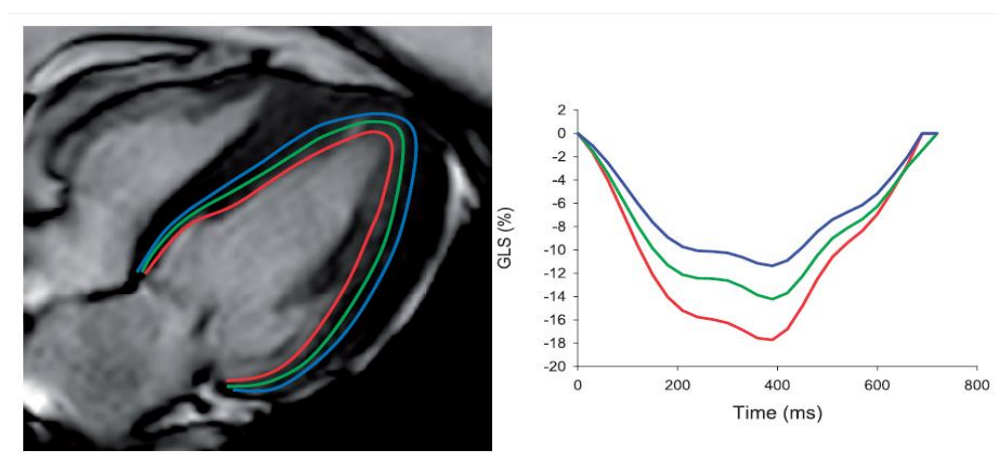


Figure 4: Different myocardium inner boundary (endocardium) segmentation (right) affecting the estimated global longitudinal strain (GLS) (left) (AMZULESCU, DE CRAENE, *et al.*, 2019).

Beyond the time-consuming challenges posed by currently used global and local parameter quantification techniques, feature tracking methods performance is subjected to additional sources of errors in CMR images. The interior of the myocardium presents highly homogenous brightness intensity in MRI, which reduces the chances of patterns of features to be tracked (AMZULESCU, DE CRAENE, *et al.*, 2019). Frequently, the boundaries of the myocardium, are used as features to be tracked along the cardiac cycle, which reduces the tracking accuracy because of the difficulties to determine the endocardium and epicardium contours (HUI WANG, AMINI, 2012).

Myocardium deformation (strain) can be evaluated as a global and local parameter and offers more information to accurately determine a patient's prognostic, besides ejection fraction, especially in chronic systolic heart failure (ZHANG, FRENCH, *et al.*, 2014). However, many inter- and intra-modality inconsistencies limit the wide use of strain in clinical routine. In the work published by Amzulescu *et al.* (AMZULESCU, DE CRAENE, *et al.*, 2019), the authors pointed out that strain quantification's main limitations involve the variation of strain value among methods, image acquisition modalities, vendors, and software versions.

To overcome the limitation posed by the variability in quantifying strain of the left ventricle, an alternative approach involves the utilization of an automated tool. In this regard, deep learning (DL), a subfield of machine learning, has emerged as a highly promising method for automating various tasks within the medical field. DL exhibits significant potential, avoiding the requirement for human interaction, and has found successful applications in diverse areas, including segmentation (AVENDI, KHERADVAR, *et al.*, 2016, MORENO, DE SÁ REBELO, *et al.*, 2019, TRAN, 2016) and motion estimation (DOSOVITSKIY, FISCHER, *et al.*, 2015, ILG, MAYER, *et*

al., 2017, SUN, YANG, et al., 2018). The adoption of DL methods can improve the performance of global and local myocardium parameter quantification, with potentially less variation, since it does not rely on human interaction and subjectivity. The inference generated from a trained DL model is deterministic, which means the same image analyzed multiple times generates the same results, ensuring consistency. Moreover, full automation of the process with DL can generate results much faster than the current techniques.

### 1.1. Objectives

In this study, we proposed and evaluated a new method based on DL to quantify myocardial strain in CMR with pulse sequence 2D-SSFP. We developed a hybrid pipeline (Figure 5) which combines both supervised and unsupervised DL techniques to automate the tasks involved in cardiac muscle segmentation and its motion estimation. We investigated the generalizability of a supervised DL segmentation method to delineate the cardiac muscle and used an unsupervised DL model to track motion in the left ventricle in real and synthetic 3D cine magnetic resonance images. Finally, we investigated the relationship between the segmented myocardium and the estimated motion to quantify myocardial strain.

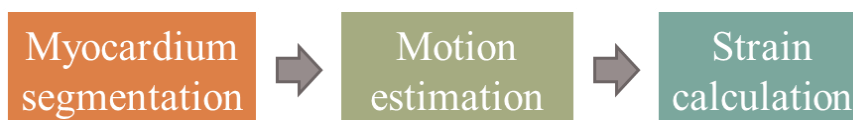


Figure 5: Proposed hybrid pipeline encompasses both supervised (myocardium segmentation) and unsupervised DL modules (motion estimation), along with an analytical module for Strain quantification.

## 2. BACKGROUND

### 2.1. Magnetic resonance image

Subatomic particles exhibit an intrinsic rotational motion around their axis, called spin. Protons are electrically charged particles, so they have a magnetic dipole moment oriented in the direction of the normal plane of spin motion. Due to the magnetic dipole in the charged particles, they tend to align themselves under the effect of an external magnetic field in the same direction as the field (WEBSTER, 2010).

Depending on the atom, the protons and neutrons of the nucleus cancel the magnetic moments between them. However, nuclei with an odd number of protons and neutrons have a resultant magnetic moment and spin different from zero, as is the case of hydrogen atoms, which consists of a single proton. Hydrogen nuclei are used for magnetic resonance imaging because of their magnetic susceptibility and their vast amount in the human body (DARTON, IONESCU, *et al.*, 2019, WEBSTER, 2010).

Particles have two normal states called parallel and antiparallel. The number of particles in the parallel state is higher than in the antiparallel state as it is the lowest energy state. Thus, a radiofrequency (RF) pulse with photons causes changing in the state of some particles to the antiparallel. The energy difference between the two states is relative to the precession frequency, or Larmor frequency,  $\omega = \gamma B$ , where  $\gamma$  is the intrinsic gyromagnetic constant of each atom, and  $B$  is the magnetic field. By applying an RF pulse, the particles resonate with the radiofrequency field and absorb energy. Figure 6a shows a schematic of this process (DARTON, IONESCU, *et al.*, 2019, WEBSTER, 2010).

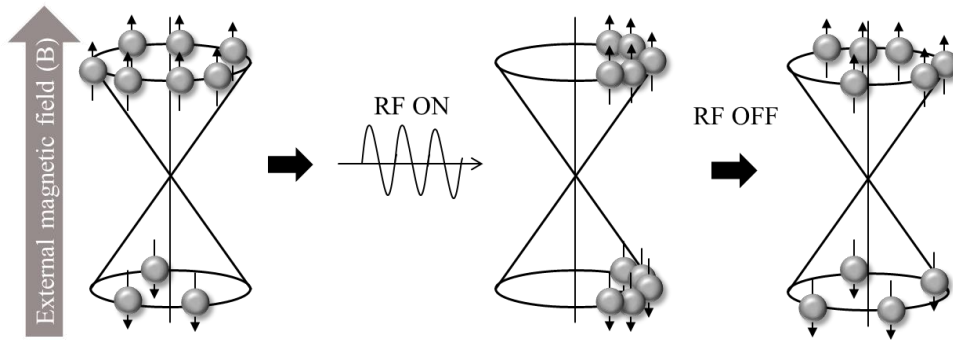


Figure 6: Protons have parallel (low energy) or antiparallel (high energy) states related to the external magnetic field (B). The population of protons in a high-energy state increases (longitudinal magnetization decreases) when a RF pulse is irradiated and the protons begin to precess in phase (increase in transverse magnetization). The protons return to their original condition when the RF pulse is turned off. Longitudinal magnetization recovers (adapted from DARTON, IONESCU, *et al.*, 2019).

When the radiofrequency pulse ends, the particles return to their original energy state, releasing the energy that was absorbed. The released signal is called Free Induction Decay (FID) and is detected by receiver coils. The time taken for the particle to return to its original state is the measure used to compose the image. The return can be divided into two temporal components, a longitudinal, T1, called spin-lattice, and a transversal, T2, called spin-spin, both vary according to the type of particles in the material (DARTON, IONESCU, *et al.*, 2019, WEBSTER, 2010).

Gradient coils are responsible for creating small variations in the magnetic field along the orthogonal axes gradually, as the resonance of the particles occurs very precisely, the gradient variation allows the excitation of particles in an organized way, in such a way that cuts in the volume can be performed, according to the gradient variation on the axis (WEBSTER, 2010).

Different image acquisition protocols can be generated by varying the application of the radiofrequency pulse, both in the direction of the pulse and in the frequency of

application, and specific results can be obtained for each type of pathological analysis application.

## 2.2. Cardiac anatomy

The heart is primarily responsible for pumping oxygenated blood to the body's various organs and tissues. The heart, as illustrated in Figure 7, is essentially comprised of two separate pumps: the right side of the heart, responsible for sending blood to the lungs, and the left side, which pumps blood to the body's peripheral organs. Both of these heart sides are pump systems with two chambers, including an atrium and a ventricle. The atrium serves as an initial pump to transfer blood into the ventricle, assisting in its movement. In contrast, the ventricles are the primary force behind propelling blood either through the pulmonary circulation, originating from the right ventricle, or through the peripheral circulation, starting from the left ventricle (HALL, GUYTON, 2011).

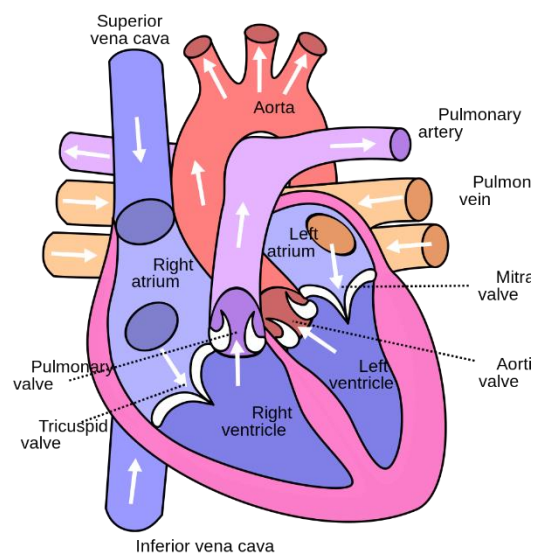


Figure 7: scheme of the heart structure (WAPCAPLET, 2003).

The left ventricle receives oxygenated blood from the left atrium and contracts forcefully to eject this oxygen-rich blood into the aorta, the largest artery in the body. From the aorta, the freshly oxygenated blood is distributed to every cell and tissue, nourishing them and providing them with the oxygen needed for their metabolic activities. The left ventricle's ability to generate this high-pressure force is vital for maintaining the body's overall health and functionality.

The left ventricle's importance is accentuated by its endurance and consistency in maintaining this high-pressure pumping throughout a person's entire life. However, it can be susceptible to various cardiac conditions, such as hypertrophic cardiomyopathy or heart failure, which can impair its ability to function effectively. The study and understanding of the left ventricle's anatomy and function are crucial for clinicians and researchers in their efforts to diagnose, treat, and prevent heart-related diseases, ensuring the continued well-being of individuals. In essence, the left ventricle serves as a testament to the heart's remarkable adaptability and unwavering commitment to sustaining human life.

### **2.3. Deep learning**

In general, Artificial Intelligence (AI) is a study field that aims to understand and develop an intelligent system that can automate the decision-making process (RUSSELL, NORVIG, 1995). According to Goodfellow, Bengio, and Courville, the AI field can be subdivided into other fields and methods (Figure 8), such as machine learning, a technique that can learn and improve with experience and data. An

artificial neural network is a type of machine learning algorithm, inspired by the basic principle of biological neural processing. Deep learning is a deep artificial neural network that learns from a vast amount of data, representing the learning problem as a hierarchy of concepts, extracting features from less complex representations to more abstract ones (GOODFELLOW, BENGIO, *et al.*, 2016).

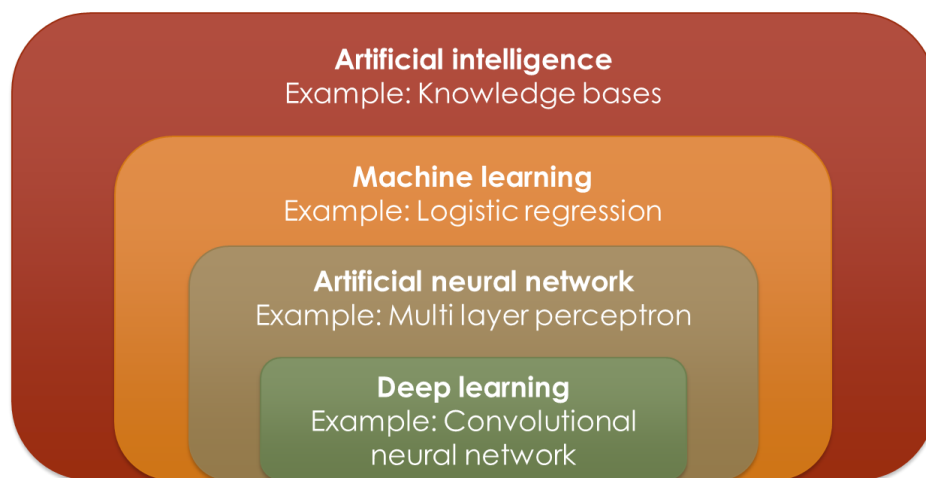


Figure 8: Relationship between different AI techniques and an example of each technique.

The basic unit of neural networks is called a neuron, which is activated or deactivated depending on the activation function and the weights learned by the network for each input. A basic network, called a multilayer perceptron (MLP) network, Figure 9, is essentially composed of neurons (nodes) with respective synaptic weights. The activation of each neuron is based on a non-linear activation function, the network has a high degree of connectivity between neurons, presenting one or more hidden layers at both the input and the output (HAYKIN, 2008).



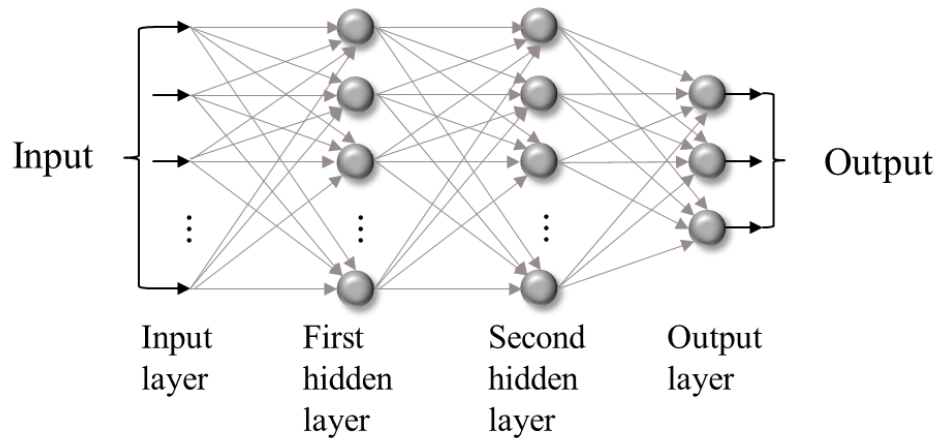


Figure 9: MLP architecture example, with two hiding layers (adapted from HAYKIN, 2008).

Mathematically a neuron can be modeled using the equation 1. The output  $y_k$  of each neuron ( $k$ ) is a composition of the sum of all synaptic weights ( $w_k$ ) multiplied by the input  $x$  and added to a bias term ( $b_k$ ), and then limited by an activation function ( $\varphi(\bullet)$ ) (HAYKIN, 2008).

$$y_k = \varphi \left( \sum_{j=1} w_{kj} x_j + b_k \right) \quad 1$$

A particular class of neural network, the convolutional neural networks (CNN), which apply convolution operations on images, have been widely used in various medical imaging applications, such as segmentation, classification, image registration, and object detection, among others (LITJENS, KOOI, et al., 2017). The main advantage of using CNNs over classical methods is the ability of networks to learn features extracted from a large volume of information, that is, learning directed from data.

A convolution is an operation between two functions, usually the input and the kernel, where the elements of the input are multiplied (element-wise) by the kernel and summed up, as exemplified in Figure 10. In the neural network field, the use of convolution often refers to the cross-correlation operation, the difference between the

two operations is the kernel orientation; however, it is not relevant to the neural network implementation. Equation 2 shows a two dimension convolution operation as used in the neural network field (GOODFELLOW, BENGIO, *et al.*, 2016).

$$(K * I)(i, j) = \sum_m \sum_n I(i + m, j + n)K(m, n) \quad 2$$

Where  $K$  is the kernel,  $I$  is the input image,  $i$  and  $j$  are indexes of the input image, and  $m$  and  $n$  are the indexes of the kernel.

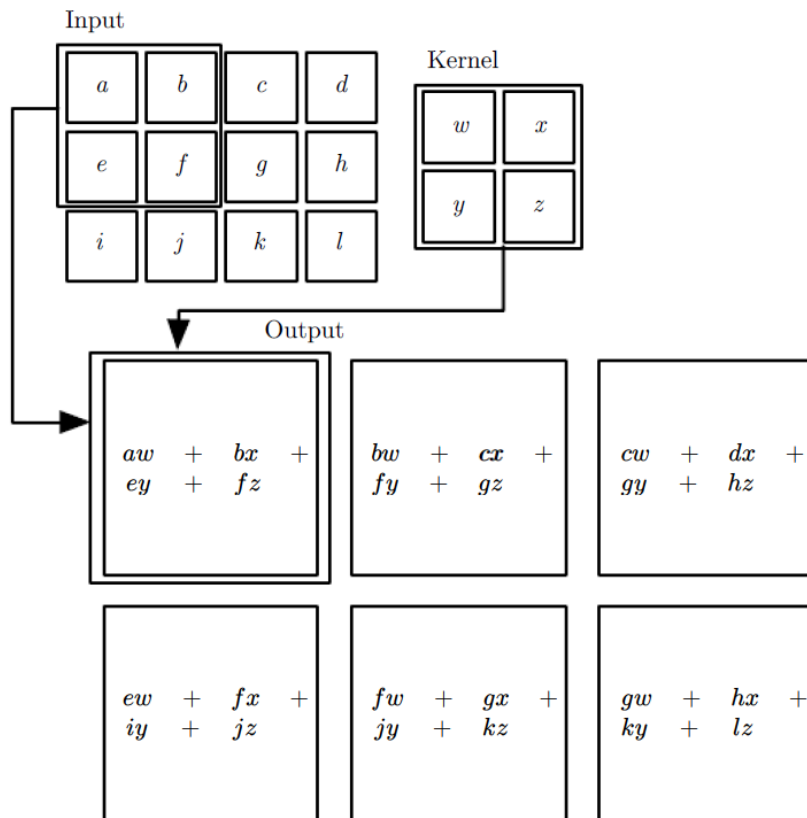


Figure 10: Example of 2D convolution operation as used in neural network. The operation performed in this example reduces the input size (GOODFELLOW, BENGIO, *et al.*, 2016).

In a 2D CNN to process images, the input of Figure 10 can be the input image or the feature map extracted from the previous layer; the kernel is the learned filter, where

each element of the kernel is a neuron; the output in Figure 9 is the feature map extracted by the learned filter.

Convolutional neural networks are usually composed of several layers, each containing a varied number of convolutional filters, which will be learned by the network. Followed by dimensionality reduction layers, called pooling, which reduce the feature maps by applying a summary statistic in the nearby elements, such as selecting the maximum value within the pooling window (max-pooling), or averaging the elements in the pooling window (average-pooling). An example of a max-pooling operation is presented in Figure 11.

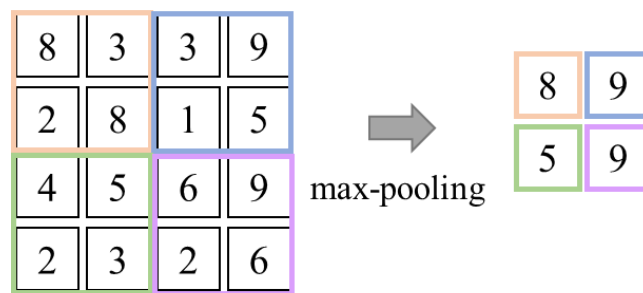


Figure 11: Example of max-pooling operation with a 2x2 window.

In the case of classification, there are layers called fully connected, which are composed of fully connected neurons, going to the dimension of the prediction vector, Figure 12 shows the general scheme of a convolutional neural network (CHEN, QIN, et al., 2020).

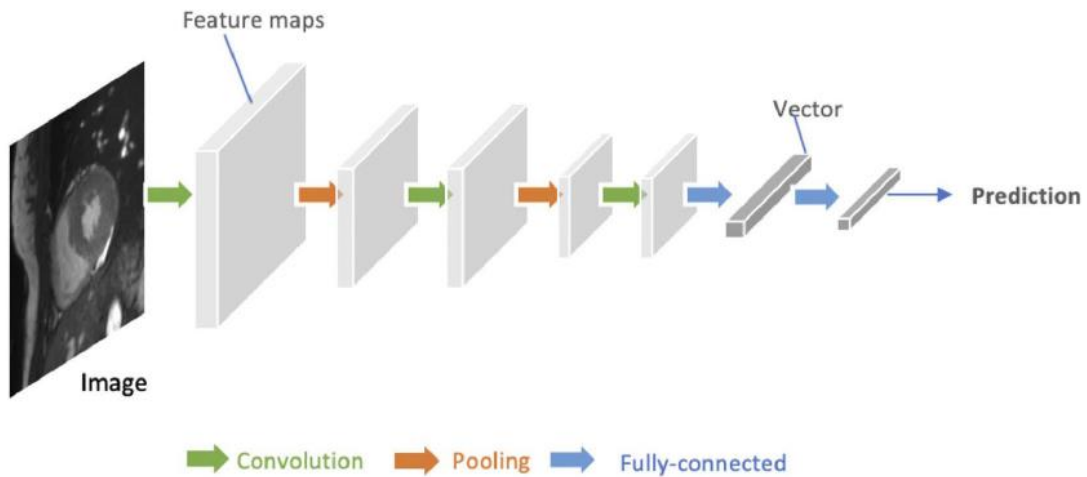


Figure 12: Simple scheme of a CNN composed of convolutions, pooling, and fully connected layers (CHEN, QIN, et al., 2020).

## 2.4. Myocardium segmentation

In recent decades, several semi- and automatic solutions have been proposed to the problem of myocardium segmentation in CMR images, usually involving models based on previous knowledge of the problem, such as anatomy, location of the left ventricle, threshold values, and in several cases requiring interaction with an experienced user (BERNARD, LALANDE, et al., 2018, COLLETTI, 2019, SUINESIAPUTRA, COWAN, et al., 2014).

There are many sources of variation in CMR imaging, some examples can be seen in Figure 13, such as anatomical variation among patients and different pathologies; image quality relating to acquisition machines and manufacturers; and others (BERNARD, LALANDE, et al., 2018).

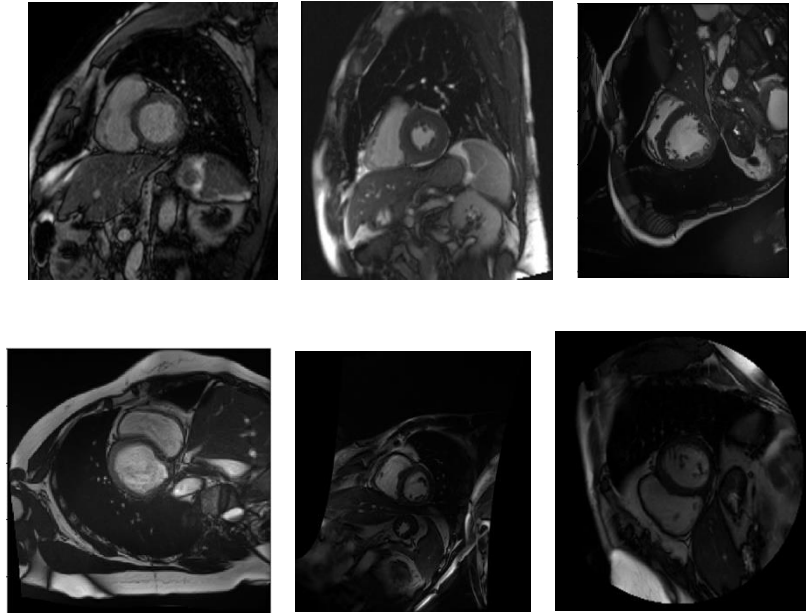


Figure 13: Variation among CMR images.

In a review of cardiac imaging segmentation methods, Petitjean and Dacher (2011) point out that the results of the available segmentation methods still need improvement. There is also an indication that the automated myocardial delineation techniques incorporated in commercial software are very sensitive to image quality and acquisition protocol (MARINO, VERONESI, et al., 2014).

## 2.5. Cardiac movement in CMR images

In computer vision, the pattern of the apparent movement of objects, surfaces, and edges in a visual scene caused by the relative movement between the viewer and the scene is defined as optical flow (OF), which is applied to all pixels. The use of optical flow in CMR is limited due to the characteristic homogeneity of pixel intensities inside the myocardium, reducing the accuracy of the method. Thus, the most used technique to determine cardiac movement in cine-CMR images is called feature tracking, which

is based on following gray patterns in small windows in images acquired sequentially in time, as shown in Figure 14. The edges of the endocardium and epicardium are the easiest patterns to follow compared to the rest of the cardiac muscle. This reduces the ability to estimate regional movement in the myocardium, as the measured displacement is concentrated on the muscle walls and not inside.

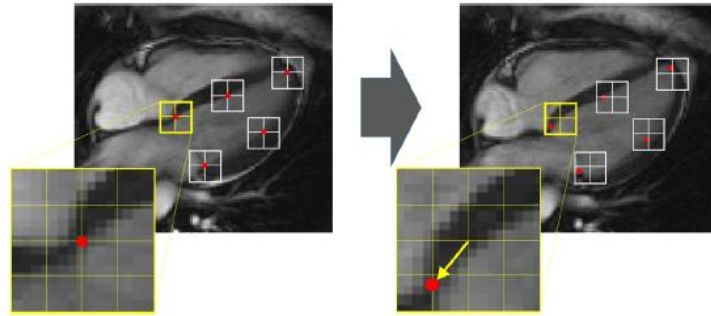


Figure 14: Basic concept of feature tracking in CMR images. This technique consists of determining small squares in the first image (left) and then looking for the possible displacement of the gray pattern in the next image (right) (PEDRIZZETTI, CLAUS, *et al.*, 2016).

Moreover, this technique generates inconsistencies between manufacturers due to problems of consensus in defining the myocardial edges, as discussed above, reducing reproducibility (PEDRIZZETTI, CLAUS, *et al.*, 2016, VOIGT, CVIJIC, 2019)

## 2.6. Cardiac strain

Cardiac deformation ( $\epsilon$ ), also called strain, is a measure derived from myocardial movement. In one-dimensional (1D) objects strain is defined as the difference between the maximum length ( $L$ ) and initial length ( $L_0$ ) over the initial length, as shown in equation 3 (SCATTEIA, BARITUSSIO, *et al.*, 2017).

$$\varepsilon = \frac{L - L_0}{L_0} \quad 3$$

There are two ways to calculate the strain: (1) displacements are calculated by fixing a point in the myocardium and computing the deformation from it, called a Lagrangian or instantaneous strain, and (2) called Eulerian or natural strain, displacements are calculated by varying the reference point, and at the end, all variations are added (D'HOOGHE, 2000, SCATTEIA, BARITUSSIO, *et al.*, 2017). Equation 4 shows the Lagrangian strain. The Eulerian strain (equation 6) is the sum of the total strain variation (equation 5) between the initial instant and the t instant.

$$\varepsilon(t) = \frac{L(t) - L(t_0)}{L(t_0)} \quad 4$$

$$d\varepsilon(t) = \frac{L(t) - L(t - dt)}{L(t)} \quad 5$$

$$\varepsilon(t) = \int_{t_0}^t d\varepsilon(t) \quad 6$$

With  $L(t)$  the length at the time instant t,  $L(t_0)$  the length at the initial time instant, and  $dt$  and  $d\varepsilon$  the infinitesimal interval of time and strain, respectively.

Figure 15 illustrates the two ways to compute the strain, Lagrangian (left) and Eulerian (center), along with a global longitudinal strain graph comparing both along the cardiac cycle (right), as can be seen in the graph, the choice of strain calculation is also a source of variation in the final result (AMZULESCU, DE CRAENE, *et al.*, 2019).

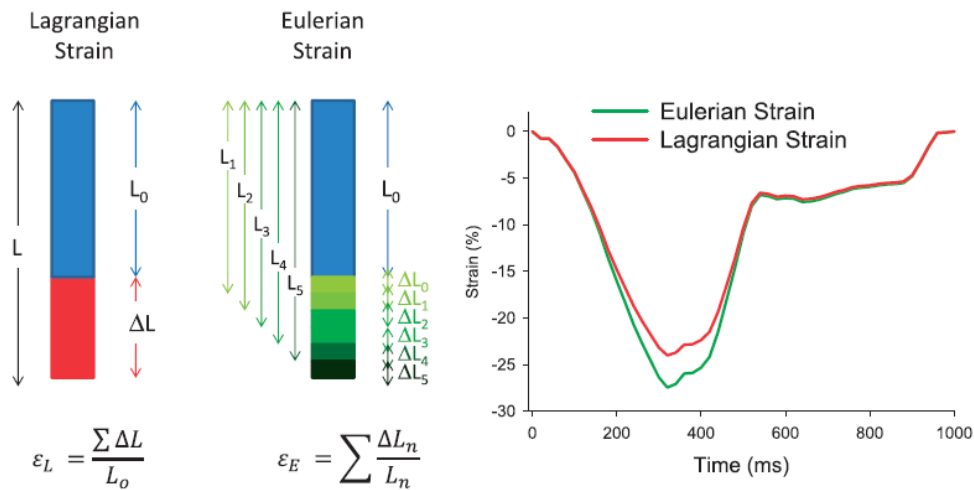


Figure 15: Different ways to calculate strain: Lagrangian (left) and Eulerian (center); And the difference in the strain curve along the cardiac cycle depending on the calculation used (right) (AMZULESCU, DE CRAENE, *et al.*, 2019).

In cardiac applications, the amount of movement between systole and diastole is significantly large, so it is more suitable to use the Eulerian strain, so the calculation is done between consecutive time instants, reducing possible calculation errors with large displacements. The use of the Eulerian strain also reduces possible variations in the definition of the initial length (D’HOOGE, 2000).

In two-dimensional (2D) or three-dimensional (3D) objects, the complete description of the deformation involves knowledge of all strain components. In the three-dimensional case, there are three normal components, one in each direction ( $x$ ,  $y$ , and  $z$ ), and six shear components. The deformation gradient tensor ( $F$ ) is determined using the partial derivatives of the displacement vector field ( $\phi$ ) in each direction,  $x$ ,  $y$ , and  $z$  (CURIALE, BERNARDO, *et al.*, 2021, D’HOOGE, 2000, SIMPSON, KEEGAN, *et al.*, 2013, SUEVER, WEHNER, *et al.*, 2017), as shown in equation 7.



$$F = \begin{pmatrix} \frac{\partial \phi_x}{\partial x} & \frac{\partial \phi_x}{\partial y} & \frac{\partial \phi_x}{\partial z} \\ \frac{\partial \phi_y}{\partial x} & \frac{\partial \phi_y}{\partial y} & \frac{\partial \phi_y}{\partial z} \\ \frac{\partial \phi_z}{\partial x} & \frac{\partial \phi_z}{\partial y} & \frac{\partial \phi_z}{\partial z} \end{pmatrix} \quad 7$$

The strain tensor ( $E_C$ ) in Cartesian space is determined according to equation 8, using the deformation gradient  $F$  (CURIALE, BERNARDO, *et al.*, 2021, SUEVER, WEHNER, *et al.*, 2017).

$$E_C = \frac{1}{2}(F^T F - I) \quad 8$$

Cardiac strain is a three-dimensional tensor characterized by the change in length and direction of defined segments at each point of the myocardium. For each point, an orthogonal coordinate system is defined concerning the geometry of the left ventricle (LV), describing the Radial, Longitudinal, and Circumferential components (SIMPSON, KEEGAN, *et al.*, 2013). The circumferential component ( $\hat{C}$ ) is tangent to the epicardium surface in the LV short-axis plane and counterclockwise direction (base view). The longitudinal component ( $\hat{L}$ ) is tangent to the epicardium surface in the longitudinal plane and grows from the Apex to the base. The Radial component ( $\hat{R}$ ) is perpendicular to the endocardium surface and points outward (MOORE, LUGO-OLIVIERI, *et al.*, 2000), Figure 16 shows a diagram with the components at an arbitrary point in the myocardium.

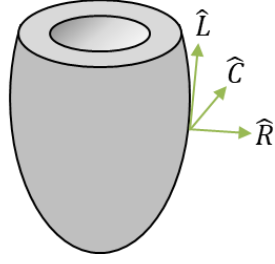


Figure 16: Illustration of longitudinal ( $\hat{L}$ ), radial ( $\hat{R}$ ), and circumferential ( $\hat{C}$ ) components in a point in the left ventricle surface.

At each point, the combination of the local coordinate system forms the rotation matrix  $\Theta$  (equation 9). To convert the strain tensor  $E_C$  to the local coordinates ( $E_L$ ) of the myocardium, equation 10 (CURIALE, BERNARDO, *et al.*, 2021, SUEVER, WEHNER, *et al.*, 2017) is applied.

$$\Theta = \begin{pmatrix} r_x & c_x & l_x \\ r_y & c_y & l_y \\ r_z & c_z & l_z \end{pmatrix} \quad 9$$

$$E_L = \Theta^T E_C \Theta \quad 10$$

## 2.7. Parameters visualization

The easy visualization of cardiac parameters, such as strain, is very important clinically, allowing for a faster and more accurate diagnosis. In addition, communication between different modalities is simplified by displaying standardized information. To standardize the visualization of cardiac parameters, the American Heart Association (AHA) developed a guideline that allows the construction of a polar map that shows important segments of the LV. Figure 17 shows a diagram of the

location of the segments and their respective nomenclature used by AHA (CERQUEIRA, WEISSMAN, et al., 2002).

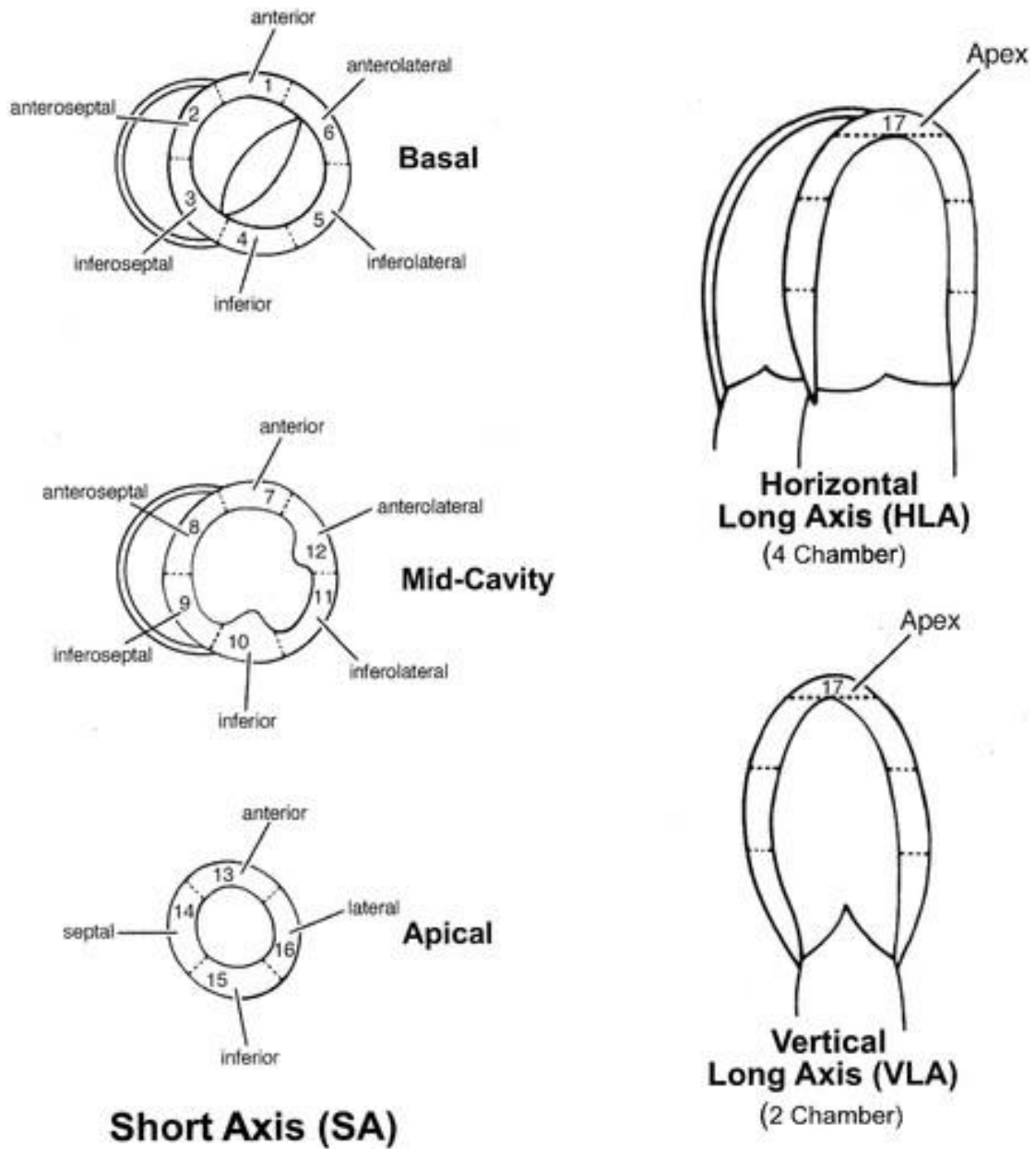


Figure 17: Diagram of standardized LV segments definition proposed by AHA and its respective nomenclature, indicating the anatomical position of the segment (CERQUEIRA, WEISSMAN, *et al.*, 2002).

The segments can be combined in a polar map form of visualization. Figure 18 shows a polar map proposed by the AHA with the respective segment's nomenclatures.

### Left Ventricular Segmentation

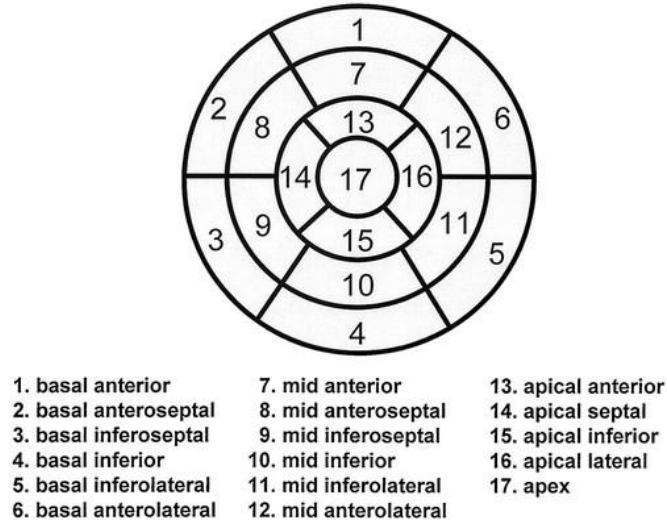


Figure 18: Polar plot used to standardize the displaying of cardiac information by AHA, showing the position of the 17 myocardial segments and its nomenclature (CERQUEIRA, WEISSMAN, *et al.*, 2002).

## 3. LITERATURE REVIEW

### 3.1. CNN generalization in myocardium segmentation

Short-axis CMR automatic LV segmentation has substantially improved with CNNs in recent years (AVENDI, KHERADVAR, *et al.*, 2016, BERNARD, LALANDE, *et al.*, 2018, MORENO, DE SÁ REBELO, *et al.*, 2019, TRAN, 2016). Although different network architectures and methods proposed in the recent articles achieved great results in the same dataset, the generalization of the methods to other datasets is

insufficiently explored. To use automatic methods in the clinical routine it must be reliable with data from multiple sources, and not overfitted in only one dataset.

In general, the segmentation learning process with CNN is performed with labels previously annotated by an expert professional, that is, supervised learning. Ideally, to achieve good generalization, the training data should contain as much heterogeneity as real-world data. Recently some works have attempted to create public heterogeneous datasets to segment the LV in CMR short-axis images (BERNARD, LALANDE, *et al.*, 2018, CAMPELLO, GKONTRA, *et al.*, 2021, PETERSEN, MATTHEWS, *et al.*, 2015). Due to the many sources of variation in CMR, including all possible different images in a dataset is virtually impossible.

The use of a large dataset was explored by Bai *et al.* (2018) in an attempt to improve the generalization of LV segmentation. The dataset used by the author contains 4,875 exams (PETERSEN, MATTHEWS, *et al.*, 2015). The Dice score obtained in the test set from the same dataset used in the training phase was very good, with 0.88 in the myocardium. However, the proposed method tested in two unseen datasets achieved a Dice score in the myocardium of 0.56 and 0.65. The authors proposed to perform fine-tuning, that is, a new training with each dataset using pre-trained weights, which is not feasible in real life since it requires the creation of a new dataset in each clinical site.

According to the authors of (KHENED, KOLLERATHU, *et al.*, 2019), a network with fewer parameters is less prone to overfitting the train data. To improve generalization, they employed a small network containing residual connections. They also used Spatio-temporal analysis as a pre-process to select the region of interest (ROI). In the same dataset as the one they trained on, their algorithm was able to get a myocardium Dice score of 0.84, and 0.82 in an unseen dataset.

Chen et al. (CHEN, BAI, *et al.*, 2020) proposed a planning data normalization and augmentation procedures to account for typical scenarios in multi-site, multi-scanner clinical imaging data sets, they used a U-net based architecture and a large dataset containing 3,975 in the training set and tested in two other datasets. They were able to achieve an average myocardium Dice of 0.82 on the external datasets.

In (GRAVES, MORENO, *et al.*, 2020) we investigate the capability of a pre-process of histogram equalization to improve the generalization in segmenting the myocardium using a CNN. We use a U-net architecture (RONNEBERGER, FISCHER, *et al.*, 2015) to perform cross-dataset training and test in 5 different datasets. Using Contrast limited adaptive histogram equalization (CLAHE) resulted in an average Dice score of 0.86 in the epicardium and 0.82 in the endocardium.

The authors of (ABDELTAWAB, KHALIFA, *et al.*, 2020) developed an approach to segment the LV that includes ROI extraction using CNNs, a novel CNN architecture for cardiac segmentation, and the incorporation of a radial loss function. They evaluated the generalizability of their method by testing it on a separate dataset, achieving a myocardium Dice score of 0.85 on a private dataset different from the public dataset used during the training phase.

To improve generalizability, the authors of (PENSO, MOCCIA, *et al.*, 2021) developed a novel CNN skip connection that includes dense blocks. They trained and tested on different databases, both private, with different acquisition equipment. The training set was composed of 210 cine sequences, and the different database used to test the model with 12 healthy volunteers. The myocardium Dice score obtained reported by the authors in the test database was 0.85.

Ribeiro and Nunes (RIBEIRO, NUNES, 2023) created a fully automatic hybrid strategy that combines DL and level set techniques to increase the generalizability of

their method for LV segmentation. They proposed new level set energy concepts by incorporating anatomical constraints and exam-specific statistical information obtained from DL segmentation. The generalizability of the method was evaluated on different configurations, using two public available datasets and one private. The model was trained on each data base and test on the remaining two. The average Dice score obtained for the endocardium contour vary from 0.77 to 0.90 and for the epicardium the Dice obtained was from 0.81 to 0.94, depending on the training and test combination.

Although the previously described papers address the problem of generalizability, further testing on larger and more diverse datasets would be necessary to fully assess generalizability and potential for clinical application of automatic LV segmentation methods based on DL.

The U-net architecture proposed by Ronneberger (2015) allows high-performance segmentation results, especially because of its concatenation paths, also called skip connections, between the downsampling and up-sampling paths. These skip connections reduce the amount of information to be learned by the network in each up-sampling level, which allows a quick convergence. Because of the U-net quickly convergence and good results, most of the works cited before used a similar U-net architecture. Although widely used in medical image segmentation, the U-net architecture has a considerable number of trainable parameters, which can result in overfitting the model in the training set.

### 3.2. CNN to quantify cardiac movement in CMR images

Although there are several tools to estimate movement in CMR images, the accurate quantification of cardiac movement and deformation remains a challenging task (DUCHATEAU, KING, *et al.*, 2020, MORALES, IZQUIERDO-GARCIA, *et al.*, 2019, PEDRIZZETTI, CLAUS, *et al.*, 2016, VOIGT, CVIJIC, 2019). In recent years, numerous works have been published describing how to improve the optical flow technique using CNN (DOSOVITSKIY, FISCHER, *et al.*, 2015, HUANG, SHI, *et al.*, 2022, ILG, MAYER, *et al.*, 2017, SUN, YANG, *et al.*, 2018).

Dosovitskiy *et al.* (DOSOVITSKIY, FISCHER, *et al.*, 2015) proposed the first end-to-end CNN optical flow learning. Neural networks need a large amount of data to train, which, at the time, was unavailable for motion tracking. So, the authors also developed a large dataset consisting of flying chairs. They performed supervised learning in the proposed FlowNet, outperforming state-of-the-art methods. In sequence, many works have contributed to improving the prediction of optical flow in computer vision with deep learning, applying supervised (HUANG, SHI, *et al.*, 2022, ILG, MAYER, *et al.*, 2017, RANJAN, BLACK, 2017, SUN, YANG, *et al.*, 2018), unsupervised (AHMADI, PATRAS, 2016, GRAVES, MORENO, *et al.*, 2021, MORALES, IZQUIERDO-GARCIA, *et al.*, 2019, REN, YAN, *et al.*, 2017, YU, HARLEY, *et al.*, 2016) and semi-supervised learning (TU, XIE, *et al.*, 2019). Sun *et al.* (SUN, YANG, *et al.*, 2018) developed a small neural network called PWC (Pyramid, Warping, and Cost Volume) which, after supervised training, was able to determine the optical flow between two images better than traditional methods and even better than other neural networks.



The application of CNN for motion prediction in cardiac magnetic resonance images is increasing in the past years. Some works have attempted to use the CNN-predicted motion as extra information to help in another task. Xu et al. (XU, XU, *et al.*, 2018) proposed a method based on deep CMR 2D images. The portion of the muscle affected by the infarction moves in a different pattern compared to the healthy tissue, so the authors' method learned the motion field as a helper to the classification.

Qin et al. (QIN, BAI, *et al.*, 2018) proposed a method to combine the motion flow field prediction with myocardium segmentation. They developed a network composed of two branches, one to learn the motion flow, and another to learn the myocardium mask. The features of both branches are learned together. According to the authors, using the learned motion field improved myocardium segmentation.

Zheng et al. (ZHENG, DELINGETTE, *et al.*, 2019) developed a pathology classifier using different characteristics extracted from CMR images. Myocardial abnormal motion is presented in many cardiac dysfunctions, so the authors adapted a U-net to generate apparent flow between two CMR image frames. The flow information was then used as input in a logistic regression classifier with other extracted characteristics from the myocardium segmentation, such as chamber volume, ejection fraction, and others. The exams were then classified according to their pathology.

Recently, Morales et al. (MORALES, IZQUIERDO-GARCIA, *et al.*, 2019) developed a work focused on the estimation of cardiac motion using CNN. They applied a modified 3D U-net to learn the motion field between two frames of a CMR image series, in unsupervised training. The images used during training are from the public dataset called the Automated Cardiac Diagnosis challenge (ACDC) (BERNARD, LALANDE, *et al.*, 2018). In real images, it is not feasible to perform a direct evaluation of the learning motion field because of the lack of ground-truth data, so the

authors also evaluated synthetic images. Their results outperform state-of-the-art methods, they were able to achieve a Dice index of 0.73 between the myocardium mask in the diastole and the warped mask in the systole using the learned field in the ACDC dataset. In the synthetic dataset, the method achieved Dice of 0.85 and an average end-point error of 1.7 pixel between the synthetically generated motion field and the learned by the network.

### **3.3. Automatic pipeline to estimate strain with CNN-based motion quantification**

Recently, some works have applied CNN motion tracking in replacement to traditional methods before estimating strain in different imaging techniques, such as ultrasound (ØSTVIK, SMISTAD, et al., 2018) and tagged CMR (FERDIAN, SUINESIAPUTRA, et al., 2020). As an extension of the work developed by Morales et al. in CMR image movement estimation, the authors of (MORALES, VAN DEN BOOMEN, et al., 2021) applied the dense motion quantification network in strain estimation workflow in real and synthetic CMR images.

Verifying the accuracy of a strain estimation approach in real CMR images is difficult since it is hard to establish a true ground truth against which to compare the resultant strain. Morales et al. used the motion and strain computed in tagging-MR images as a source of more reliable comparison. They also compared normal ranges values of strain reported in the literature with the obtained by the proposed method (MORALES, VAN DEN BOOMEN, et al., 2021).

However, there is no consensus on the range of normal myocardium strain values. In a meta-analysis performed by Vo et al. (VO, MARWICK, et al., 2018) mean values

for global radial, longitudinal, and circumferential strain were estimated based on 659 health subjects reported in 18 papers for feature tracking method in CMR images. The mean value for global radial strain (GRS) reported is 34.1% (95% CI: 28.5% to 39.7%), for global circumferential strain (GCS) -23% (95% CI: -24.3% to -21.7%) and global longitudinal strain (GLS) around -20.1% (95% CI: -20.9% to -19.3%).

Besides the normal range compared with the literature, in our work we propose to evaluate the estimated strain with a semi-quantitative visual index called Wall Motion Score (WMS) performed by an experienced radiologist, comparing the obtained strain range with normal motion indicated by the radiologist. We also compared our results with two commercial software. Moreover, we investigate the variation of values generated by the commercial software in intra and inter-observer analyses.

#### **4. METHODOLOGY**

A hybrid pipeline that uses both supervised and unsupervised DL to automate the tasks involved in cardiac muscle segmentation and its motion estimation is presented in Figure 19 and includes three major steps: (Section 4.1) Myocardium segmentation, (Section 3.2) Motion quantification, and (Section 4.3) Strain calculation. In the following, each step will be detailed.

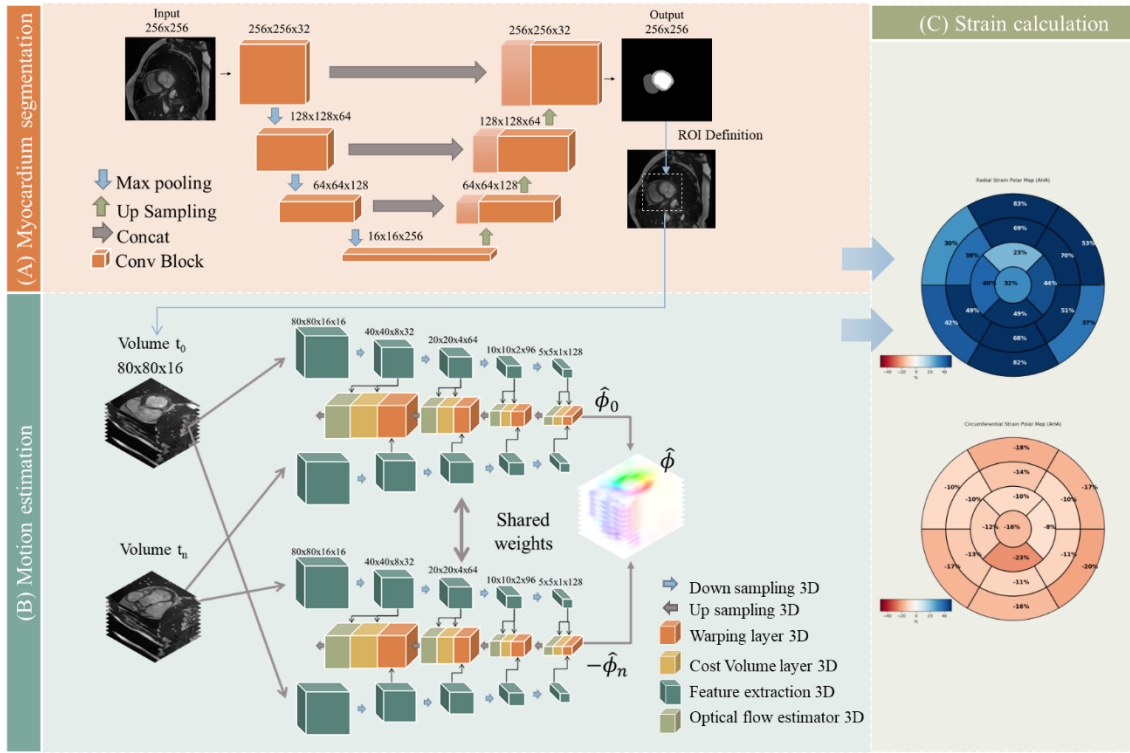


Figure 19: Strain quantification process using two input volumes of stacked CMR images at time 0 ( $t_0$ ) and time n ( $t_n$ ). With (A) the LiteResnet used to segment the myocardium and (B) the PWC Siamese network to compute the motion field from  $t_0$  to  $t_n$  ( $\hat{\phi}_0$ ) and from  $t_n$  to  $t_0$  ( $-\hat{\phi}_n$ ), creating the average motion field ( $\hat{\phi}$ ) used to determine the strain in the myocardium (C).

## 4.1. Myocardium segmentation

### 4.1.1. Network

The network used to segment the myocardium is a LiteResnet architecture (Figure 20), composed of three residual blocks in the down-sampling path. Initially, the first convolution block consists of 32 feature channels, and then it is doubled at each block. An up-sampling path follows the down-sampling path. The feature maps of the last layers of each down-sampling block are concatenated with the corresponding up-sampling block with the same dimensionality.

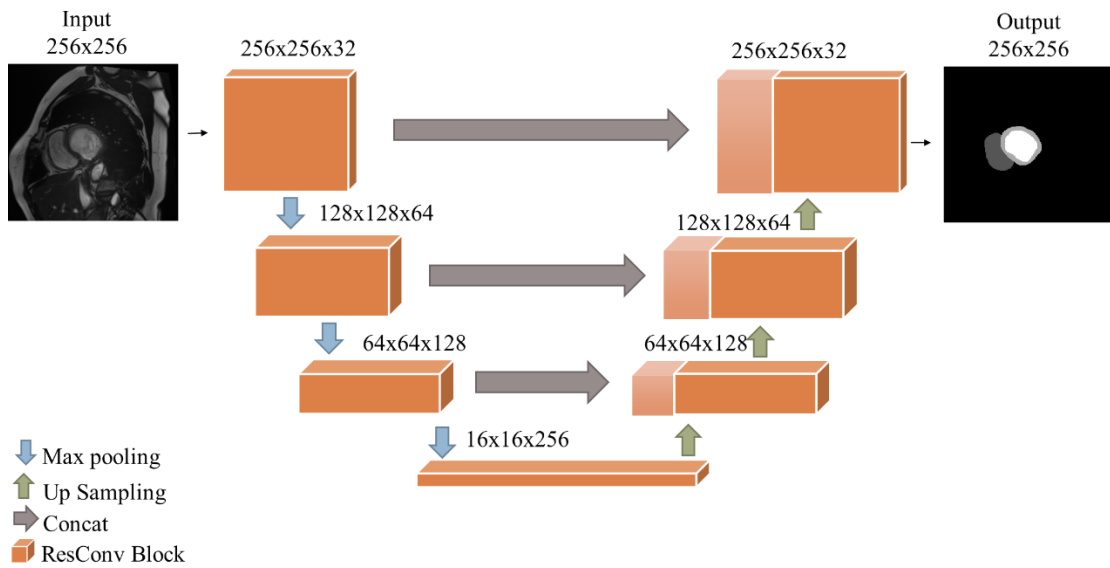


Figure 20: LiteResnet architecture used to segment the myocardium in CMR images.

Each residual block (ResConv), as shown in Figure 21 is composed of a separable convolution with a dilation rate of 1, then another dilated convolution with dilated rate of 2, and then a third separable convolution with dilation 4, the feature maps from the input of the block and the last convolution layer of the block are summed up, forming the residual connection. The activation function following all the convolution layers is the sigmoid, with exception of the last layer which is a softmax function.

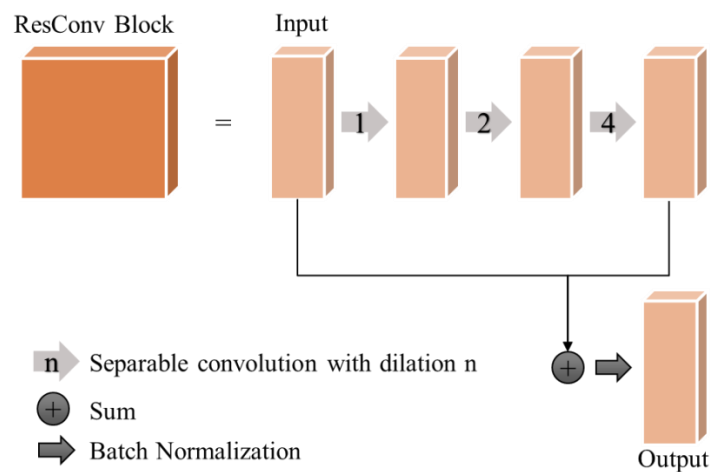


Figure 21: Scheme of the residual block used in the backbone of the LiteResnet.

Residual Network is a type of deep neural network that uses residual connections to address the degradation problem that occurs when training deep neural networks (HE, ZHANG, *et al.*, 2016). The idea of residual learning involves learning residual functions with reference to the layer inputs, instead of learning the desired underlying mapping directly, as shown in Figure 21. By using residual connections, the network can learn to preserve the information from earlier layers and combine it with the information from deeper layers. This can lead to better generalization and improved performance on various tasks.

A separable convolution layer performs the convolution in each channel individually, reducing the kernel size, and consequently reducing also the learnable parameters.

Compared to the U-net model, which consists of approximately 31 million trainable parameters, the proposed network contains around 580,000 trainable parameters. The smaller size of the proposed model is more appropriate to prevent overfitting on the training data.

The dilation convolution allows the model to extract features with a large receptive field, giving information from different locations in each layer, then summing up the features from the beginning of the block with the last block (with a large receptive field) reduces the amount of information to be learned by the model on each block.

#### 4.1.2. Data

Six different datasets, described below, were used in the experiments, all composed of 2D-SSFP short-axis CMR series. Table 1 summarizes the details of each dataset.

- A public dataset launched in the MICCAI 2017 called Automated Cardiac Diagnosis Challenge (ACDC), composed of 100 exams in the training set of

images acquired during 6 years of clinical routine. Two scanners of two different magnetic intensity fields were used to acquire the images: 1.5 T Area and 3 T Trio Tim, both from Siemens (Siemens Medical Solutions, Germany). The dataset is divided into five categories related to cardiac pathologies: normal, systolic heart failure with infarction, dilated cardiomyopathy, hypertrophic cardiomyopathy, and abnormal right ventricle (BERNARD, LALANDE, *et al.*, 2018). The exams resolutions are from 0.70 mm/pixel to 1.92mm/pixel in the xy plane, and in the z plane from 5 to 10 mm/pixel. The images sizes vary from 154 to 512 pixels and the number of slices from 6 to 18. The annotations are available for the ED and ES phases.

- A set of 59 exams acquired as part of the clinical research protocol (approved by the Institutional Review Board under #4565/17/065) at the Heart Institute (Incor) University of Sao Paulo Medical School, Brazil. The exams were acquired on a 1.5 T MRI system (Canon Vantage Titan, Canon Medical System Corporation, Japan) and classified according to the LV ejection fraction of the subject: Normal, mild/moderate dysfunction, and severe dysfunction (MORENO, DE SÁ REBELO, *et al.*, 2019). The exams dimensions vary from 192 to 216 pixels, and the number of slices varies from 7 to 11. The pixel spacing in the exams is from 1.66 mm/pix to 2.08 mm/pix and the slice thickness for all the exams is 10 mm. The annotations were performed only on the ES and ED phases.
- Dataset available as part of the MICCAI 2009 left ventricle segmentation challenge, containing 45 exams from individuals classified into four groups: healthy, LV hypertrophy (HYP), heart failure without infarction (HF), and heart failure with infarction (HF-I). The data were acquired at Sunnybrook

Health Sciences Centre, Toronto, Canada, on a 1.5T GE Signa MRI. Epi- and endocardium manual annotations are provided in different slices at ED and ES phases (RADAU P., LU Y., CONNELLY K., PAUL G., DICK A.J., 2009). The images sizes are 256 x 256 in all exams, the pixel spacing ranges from 1.21 to 156 mm/pix, and the slice thickness varies from 8 to 10 mm.

- Dataset available as part of the 2011 Left Ventricle Segmentation Challenge (LVSC) STACOM Workshop, containing 100 exams for training and 100 for validation. Exams were classified into two classes: coronary artery diseases and mild-to-moderate left ventricular dysfunction. The ground truth for each slice and phase is provided only for the training data, and it was obtained by a semi-automated segmentation technique (SUINESIAPUTRA, COWAN, et al., 2014). The image size varies from 156 pixels to 512 pixels, the number of slices from 8 to 24, and the number of phases in each exam vary from 17 to 34. The pixel spacing ranges from 0.7 to 2.08 mm/pixel and the slice thickness from 6 to 10 mm.
- The Multi-Disease, Multi-View, and Multi-Center Right Ventricular Segmentation in Cardiac MRI (M&Ms-2) dataset (CAMPELLO, GKONTRA, et al., 2021). The M&Ms-2 dataset consists of 360 exams divided into seven pathological classes and a normal class. The exams were obtained in three separate clinical locations utilizing ten distinct scanner types from three different suppliers. This dataset contains segmentation masks for the left and right ventricles in short and long-axis CMR, as well as the disease class of each individual. The exams contain volumes ranging from 6 to 28 slices, dimensions in x and y planes from 192 to 512 pixels, in-plane pix spacing from 0.6 to 1.64



mm/pixel and in the longitudinal plane from 5 to 19 mm/pixel. The annotations were performed only on the ES and ED phases.

Table 1: Datasets details

Dataset	Exams	Classes	Scanners
Automated Cardiac Diagnosis Challenge (ACDC) (BERNARD, LALANDE, <i>et al.</i> , 2018)	100	Normal (30) Systolic heart failure with infarction (30) Dilated cardiomyopathy (30) Hypertrophic cardiomyopathy (30) Abnormal right ventricle (30)	1.5 T Siemens Area 3 T Siemens Trio Tim
Instituto do Coração – HCFMUSP (INC) * (MORENO, DE SÁ REBELO, <i>et al.</i> , 2019)	59	Normal (31) Mild dysfunction (16) Severe dysfunction (12)	1.5 T Canon Vantage Titan MRI
Sunnybrook Health Sciences Centre (SUN) (RADAU P., LU Y., CONNELLY K., PAUL G., DICK A.J., 2009)	45	Healthy (9) LV hypertrophy (12) heart failure without infarction (12) Heart failure with infarction (12)	1.5T GE Signa MRI
Left Ventricle Segmentation Challenge (LVSC) (SUINESIAPUTRA, COWAN, <i>et al.</i> , 2014)	100	Coronary artery diseases Mild-to-mod. Dysfunction	1.5 T GE Signa 1.5 T Philips Achieva 3.0 T Philips Achieva 1.5 T Philips Intera 1.5 T Siemens (Avanto, Espree, and Symphony)
The Multi-Disease, Multi-View, and Multi-Center Right Ventricular Segmentation in Cardiac MRI (M&Ms-2) dataset (CAMPELLO, GKONTRA, <i>et al.</i> , 2021)	360	Normal subjects (75) Dilated Left Ventricle (60) Hypertrophic Cardiomyopathy (60) Congenital Arrhythmogenesis (35) Tetralogy of Fallot (35) Interatrial Communication (35) Dilated Right Ventricle (30) Tricuspid Regurgitation (30)	1.5 T GE (Signa Excite, Signa HDxt, Signa Explorer) 3 T GE Signa HDxt 1.5 T Philips Achieva 1.5 T Siemens (Avanto, Avanto Fit, Symphony, and SymphonyTim) 3 T Siemens TrioTim

\* clinical research protocol approved by the Institutional Review Board (IRB) under #4565/17/065

#### 4.1.3. Strategy for generalization

*Intensity homogenization:* Since the exams were obtained from different sources, all the image intensities were normalized individually between 0 and 1 to constrain all intensities to the same range. To reduce the heterogeneity of brightness and contrast among the different images, and particularly different exams, we applied a pre-processing step in each image. In the work developed previously (GRAVES, MORENO, *et al.*, 2020) we compared some image equalization pre-process methods to improve myocardium segmentation. Taking into consideration the equalization performances obtained by the investigated methods, we selected the Contrast Limited Adaptive Histogram Equalization (CLAHE) (PIZER, AMBURN, *et al.*, 1987), which applies the histogram equalization locally on small windows of 8x8 pixels and limits the contrast in each window to avoid the amplification of noises and enhance local details.

*Data augmentation:* To increase the variety of shapes during training, we generated synthetic images by applying shape transformation in the training images: resizing (0.7 to 1.5 of the original image size), rotation ( $-30^\circ$  to  $+30^\circ$ ), and random translation. All the training sets were increased 20 times after the transformations.

The size of most images in the datasets lies from 288 to 154 pixels. Therefore, all the images were adjusted into a matrix of size 256 x 256 to be inserted as input in the network. Images with smaller sizes were centered in the middle of the matrix and zero-padded to 256x256. Bigger images were centered, and the exceeding pixels (larger than 256x256) were cropped.

#### 4.1.4. Training

To compare our proposed architecture to the U-net we performed a k-fold cross-validation, using 4 folds. The ACDC dataset was divided into 5 folds randomly, then 3 folds were used to train, 1 to validate and 1 to test the models. During the training process, the training and validation sets were employed. The models were trained during 100 epochs, and to avoid overfitting, the weights that performed better in the validation set during the training phase were preserved. The loss function utilized to enhance segmentation is a linear combination of binary cross-entropy (BCE) (KHENED, KOLLERATHU, *et al.*, 2019) and Dice-based loss to decrease foreground misclassification. BCE loss is intended to reduce the error pixel-wisely, which is important for rough discrimination between background and foreground structures. However, in many medical image segmentation tasks, the object of interest is much smaller than the background, increasing the probability of misclassification of the learned mask using BCE (KHENED, KOLLERATHU, *et al.*, 2019). Thus, to improve the segmentation, the loss function was combined with a Dice-based loss (RADAU P., LU Y., CONNELLY K., PAUL G., DICK A.J., 2009). The training was performed with adaptive moment estimation (ADAM) for stochastic gradient optimization, with a learning rate of  $10^{-4}$  and a batch size of 25. Only the weights with the lowest loss in the validation set were saved to prevent overfitting in the training data.

#### 4.1.5. Evaluation

The Dice index, equation 11, was adopted to evaluate how much the predicted area overlaps with the original label. It is defined as the ratio between twice the overlapped area over the sum of both areas (MORENO, DE SÁ REBELO, *et al.*, 2019).

$$\text{Dice} = \frac{2 |M \cap \hat{M}|}{|M| + |\hat{M}|}$$

11

Where  $M$  is the ground-truth mask and  $\hat{M}$  the predicted mask.

## 4.2. Motion quantification

### 4.2.1. Network

Inspired by the PWC lightweight and the great results achieved by the network in computer vision, we developed a Siamese architecture with a modified version of the PWC in unsupervised training. The PWC network (SUN, YANG, *et al.*, 2018) is composed of 6 levels of dimensional reduction, we implemented a version with 5 levels to decrease complexity, due to the smaller dimension of our input. We also insert some batch normalization between the convolutional layers to accelerate convergence during training. The PWC network architecture implemented consists of two feature extraction paths, one for each input volume, decreasing the dimensionality of the volumes by 5 times, as shown in Figure 22. A block combining a warp transformation layer, with cost volume and optical flow estimator is applied at each level of dimensionality reduction. The optical flow field obtained at the output of each block is increased in size and concatenated into the next block.

The PWC was used as the main component of the model, so a structure called the Siamese network was created, the intermediate network (PWC) is fixed and the weights are shared between the two different processes, as illustrated in Figure 23. The reference 3D volume ( $t_0$ ) initially is used as input in position 0 of the intermediate network PWC and the moving volume ( $t_n$ ) in position 1, generating a displacement field between the reference volume and the moving volume ( $\hat{\phi}_0$ ). At the same time,

the volume of  $t_n$  is inserted into the intermediate network PWC at position 0 and the volume  $t_0$  at position 1, generating another displacement field ( $\hat{\phi}_n$ ), which in theory is the inverse of the previous one. Then, an average between  $\hat{\phi}_0$  and  $-\hat{\phi}_n$  is performed, generating an average vector field  $\hat{\phi}$ . In each vector field output, an intermediate loss function is calculated using the reference image, the learned displacement field, and the image used as moved in each case. The loss function used in network training is the average between these intermediate functions together with the smoothing function, as shown in equation 12.

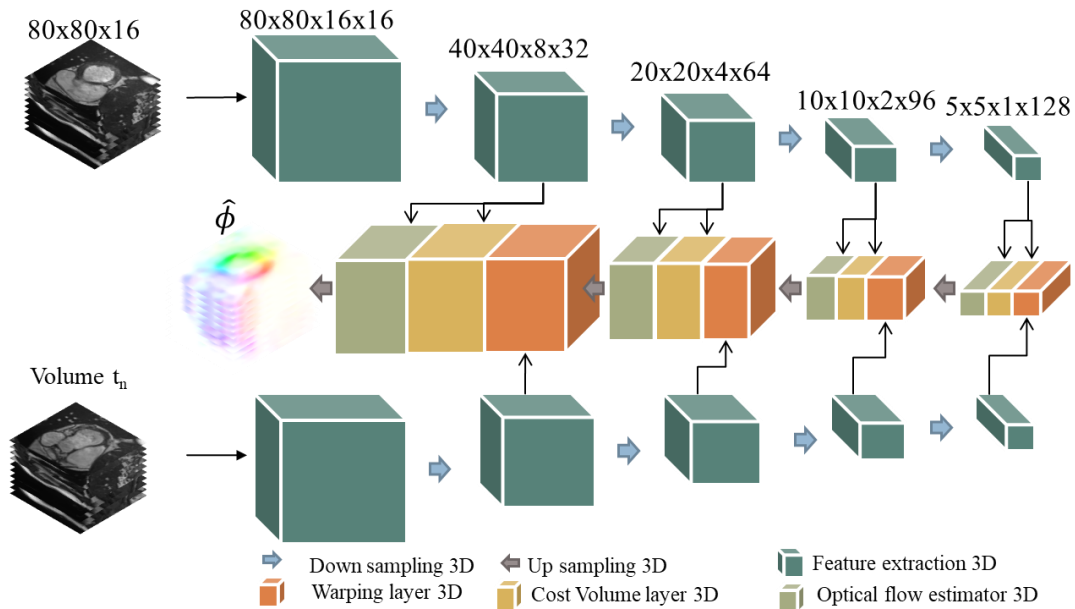


Figure 22: PWC network used as the main component of the Siamese network. Inputs are composed of two volumes acquired at consecutive frames ( $t_0$  and  $t_n$ ); Then, the images go through a series of dimensionality reduction (Downsampling) and feature extraction and warp transformation blocks, cost volume, and optical flow estimator.

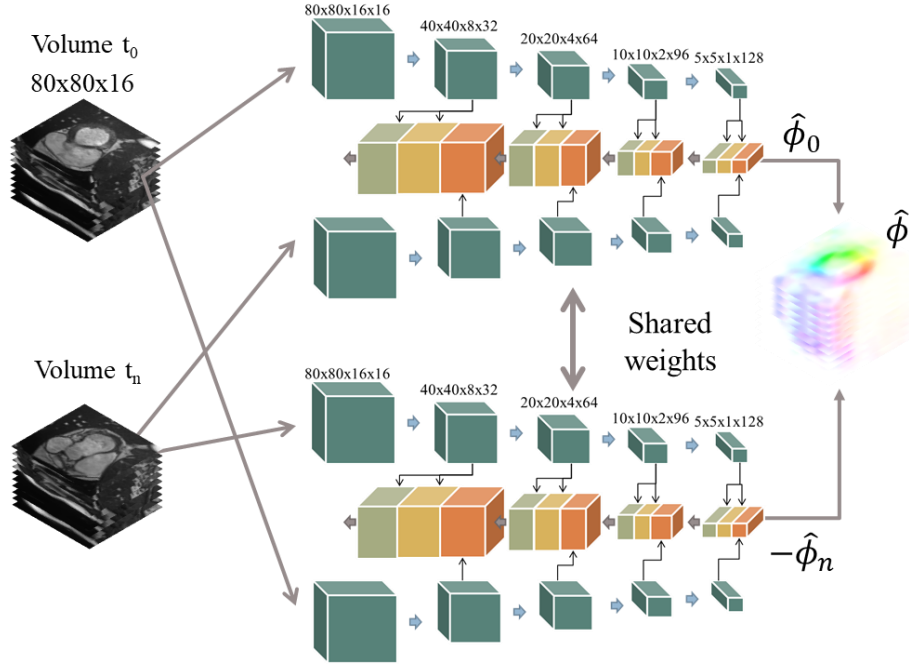


Figure 23: Siamese network architecture.

$$\mathcal{L} = \overline{dSSIM}(V, V_w) + \alpha \overline{\ell_{smooth}}(\hat{\phi}) \quad 12$$

$$dSSIM(V, V_w) = 1 - \frac{(2\mu_V\mu_{V_w} + c_1)(2\sigma_{VV_w} + c_2)}{(\mu_V^2 + \mu_{V_w}^2 + c_1)(\sigma_V^2 + \sigma_{V_w}^2 + c_2)} \quad 13$$

$$\ell_{smooth}(\hat{\phi}) = \sum_{p \in \Omega} \nabla \hat{\phi}(p)^2 \quad 14$$

Where,  $V$  is the volume in any time instant (0 or  $n$ ) and  $V_w$  is the warped volume using the referenced motion field and the other volume;  $\alpha$  is a constant, set to  $10^{-7}$ ;  $\mu$  is the average intensity of the respective volume,  $\sigma$  the variance,  $\sigma_{VV_w}$  the covariance of  $V$  and  $V_w$ ;  $c_1$  and  $c_2$  constants set to 2.55 and 7.65, respectively; and  $\Omega$  is the domain of  $\hat{\phi}$ .

#### 4.2.2. Data

Three datasets were used in the motion estimation. The training set of the ACDC dataset (described previously) was used to train the network. The INC dataset was used

to test the motion estimation. A mathematical phantom was used to create a synthetic dataset to directly compare the displacement field generated mathematically and calculated by the network since in real CMR images is very hard to obtain a ground truth displacement field.

CMR synthetic images were generated using the 4D extended cardiac-torso (XCAT) mathematical phantom (SEGARS, STURGEON, *et al.*, 2010) produced by MRXCAT software (WISSMANN, SANTELLI, *et al.*, 2014). The XCAT mathematical phantom is capable of generating synthetic images with highly detailed anatomy, as shown in an example in Figure 24 A. It possesses multiple parameters to allow the creation of different cardiac motion patterns and generates the displacement field during the simulated cardiac cycle, information that would be hardly obtained precisely in real-life measurements. Since the XCAT images are created as anatomic masks of different organs, we used the MRXCAT software to transform those images into realistic CMR. The software is built on top of XCAT and assigns magnetic resonance properties to each tissue mask. Figure 24 A shows an example of a cardiac short axis simulated in the XCAT and Figure 24 B shows the transformation of the image by the MRXCAT into a CMR acquisition type.

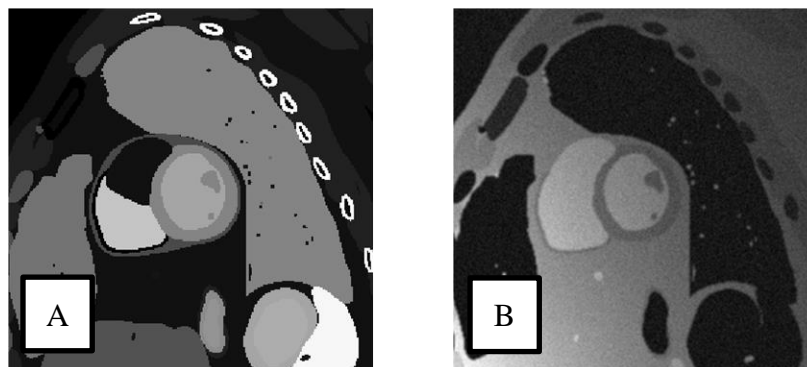


Figure 24: (A) Example of short axis cardiac image generated by the XCAT and (B) the same image transformed into a CMR pattern using MRXCAT.

### 4.2.3. Evaluation

The metrics used to evaluate the results between the ground truth displacement field, generated by XCAT ( $\phi$ ), and the predicted by the network ( $\hat{\phi}$ ) were MAE (Mean Absolute Error) and End-Point-Error (EPE), described respectively in equation 15 and 16 (MORALES, IZQUIERDO-GARCIA, *et al.*, 2019) and percentage of correct pixel (PCP), equation 17, that analyzes the percentage of pixels that present absolute percentage error bellow a threshold ( $\beta$ ), in the case, used 10%.

$$MAE = \frac{1}{N} \sum_{i=1}^N |\phi_i - \hat{\phi}_i| \quad 15$$

$$EPE = \frac{1}{N} \sum_{i=1}^N \sqrt{(\phi_{u_i} - \hat{\phi}_{u_i})^2 + (\phi_{v_i} - \hat{\phi}_{v_i})^2 + (\phi_{w_i} - \hat{\phi}_{w_i})^2} \quad 16$$

$$PCP = \frac{100}{N} \sum_{i=1}^N \begin{cases} \left| \frac{\phi_i - \hat{\phi}_i}{\phi_i} \right| < \beta & 1 \\ otherwise & 0 \end{cases} \quad 17$$

Where  $u$ ,  $v$ , and  $w$  are components of the displacement vector in  $x$ ,  $y$ , and  $z$  directions, respectively, and  $N$  is the number of pixels.

Since in real images the motion ground truth is hard to obtain, to evaluate the performance in the real images the Dice index (equation 11) was applied between the myocardium mask in the fixed position and the warped myocardium mask in the moving frame using the learned displacement field.

The results obtained were compared with two classical motion estimation techniques: 3D Lucas-Kanade Optical Flow (LUCAS, BRUCE D. AND KANADE, 1981),



implemented using Python language, and 3D B-Spline registration from the SimpleITK<sup>1</sup> 2.0.2 package for python.

### 4.3. Strain

To estimate strain, first the components  $\hat{R}$ ,  $\hat{C}$ , and  $\hat{L}$  need to be determined in each point, for that the myocardium is divided into multiple concentric contours in the plane (Figure 25). So, component  $\hat{C}$  can be easily calculated by the tangent to the contours in each point.

Initially, the myocardial mask was divided into 5 concentric contours, as shown in Figure 25.

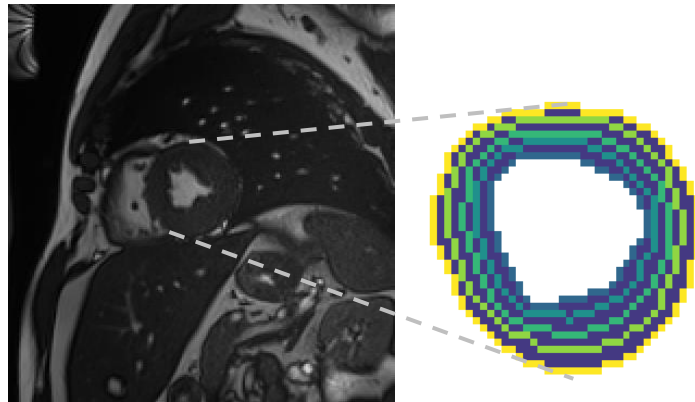


Figure 25: Example of 5 concentric contours division (right) performed in the myocardium area.

Then, the strain tensor at each point of each contour was calculated. The  $C$  component at each point was defined as the tangent to the contour at the point. The  $L$  component, to simplify the calculation, was defined as the straight line between the point itself

---

<sup>1</sup> <https://simpleitk.org/>

and its projection in the slice below. The  $R$  component was found through the cross-product between  $C$  and  $L$ .

After finding the system components, the system rotation matrix was calculated, so that the  $R$ ,  $C$ , and  $L$  system is aligned with the  $x$ ,  $y$ , and  $z$  directions of the Cartesian system. Then, the strain tensor was obtained using the equations 7 to 10.

#### 4.3.1. Data

The dataset used to assess strain quantification consists of 62 exams collected during routine clinical practice. There are 10 healthy individuals and 52 patients with various diseases among the participants. The scanners used were 1.5T Canon Vantage Titan (Canon Medical System Corporation, Japan), 1.5 GE Signa (GE Healthcare Systems, USA), and 1.5 Philips Achieva (Philips Healthcare, Best, The Netherlands).

We also used the M&Ms-2 dataset to compare our strain quantification method to that of (MORALES, VAN DEN BOOMEN, *et al.*, 2021), which was recently published.

#### 4.3.2. Evaluation

To evaluate the result in the synthetic data it was used the mean average error (MAE), which is described in equation 15.

Obtaining quantitative performance metrics to calculate strain on real cardiac MRI images is particularly difficult due to the lack of ground truth.

Three experienced professionals analyzed CMR images of 62 patients, classifying the myocardium regions in the degree of movement based on a semi-quantitative visual index called the Wall Motion Score (WMS), characterizing each of the 17 regions of the polar plot (Figure 18) into hypokinetic, akinetic, and dyskinetic. As illustrated in Figure 26, normal means that the movement of the myocardial wall presents

contraction expected for the normality pattern, hypokinetic means that the wall presents reduced movement, akinetic means no movement or very close to the absence of movement in the region, dyskinesia is when the wall moves in the opposite direction of the expected.

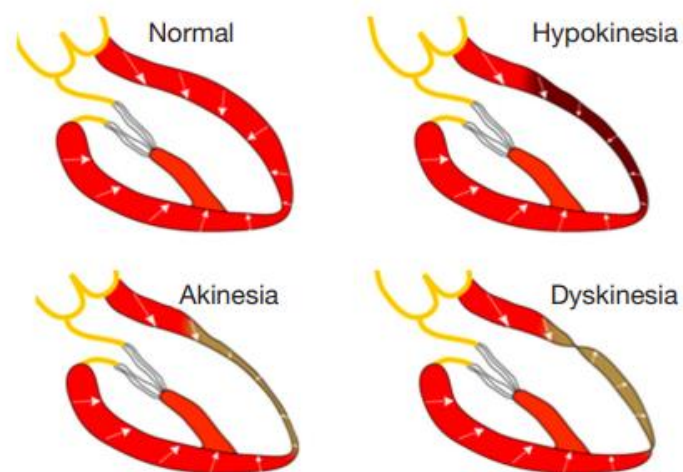


Figure 26: Illustration of the wall motion score classes: normal, hypokinetic, akinetic, and dyskinetic (LEISCHIK, DWORRAK, *ET AL.*, 2016).

Two of the professionals did the categorization, while a third, more experienced professional examined the divergences between the determined classes and decided a consensus for more reliable labeling.

Strain is an indirect measure of myocardium wall movement, so values of strain are directly related to the WMS. In the radial strain direction, as the strain value increases it is closer to normal wall motion, and it follows a linear correlation decreasing in the hypokinesia, akinesia, and dyskinesia.

The calculated strain was compared with the classical methods described before, and with two software available in the market: Circle CVI 42<sup>®2</sup> and Medis<sup>®3</sup>. Two experienced professionals generated the strain analysis in the software. A radiologist repeated the strain analyses in the commercial systems in a subset of 20 exams (10 healthy and 10 non-healthy) to explore the intra-observer variation of results in systems with the same operator at different times. Another experienced radiologist performed the strain studies in the same 20 exams to see how different observers in commercial systems affected the strain measurement.

Using the radial and circumferential strain data, a logistic regression classification system was done between the WMS classifications of normal and not normal (other classes) to better examine the potential of the proposed technique compared to the classical methods and the two commercially available methods. The investigation used cross-fold validation using four folds to estimate classification performance for various sets of data.

To compare our method to the developed by Morales et al. (MORALES, VAN DEN BOOMEN, *et al.*, 2021), we executed both pipelines on a dataset that neither method had seen before. Because the dataset lacks a strain label, one way to measure the method's efficacy is to look at its ability to distinguish between healthy and pathological participants, so the evaluation, in this case, is performed by the differences between the calculated strain along the cardiac cycle in the healthy and pathologic groups by the two methods.

---

<sup>2</sup> <https://www.circlevi.com/>

<sup>3</sup> <https://medisimaging.com/>

## 5. RESULTS AND DISCUSSION

### 5.1. Myocardium segmentation

The comparison between the U-net and the proposed LiteResnet was performed in a 4-fold cross validation experiment, training the models with the ACDC dataset. The Figure 27 shows the evolution of the average Dice score in the training set and validation set in each model during training, showing also the standard deviation across the folds.

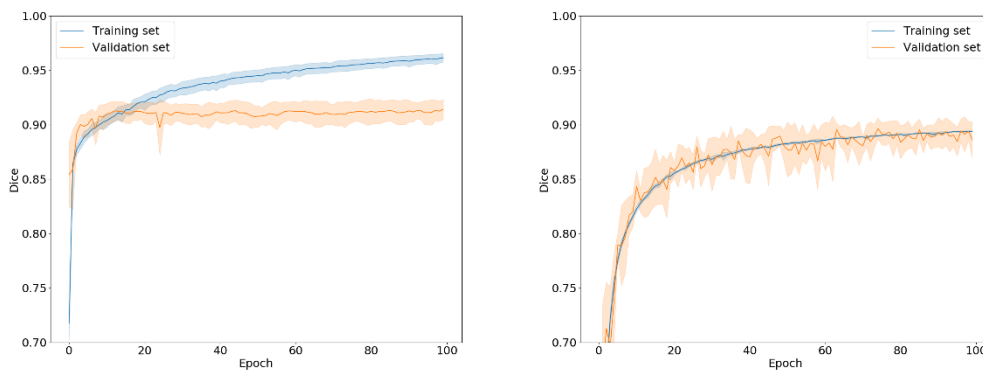


Figure 27: Average Dice score during training process of the U-net (left) and LiteResnet (right) for the training set and validation set.

The U-net experienced overfitting in the training data, as seen in Figure 27, because the Dice increased in the training set but remained constant in the validation set. The LiteResnet the Dice score in the validation set keep increasing with the training set, indicating that the model did not overfit the training data.

Table 2, Table 3 and Table 4 show the Dice scores achieved in the endocardium, epicardium and myocardium, respectively, for the test set from a distinct dataset.

Table 2: Endocardium Dice scores obtained with U-net and LiteResnet tested in set samples from the datasets ACDC, INC, SUN, LVSC, and M&Ms-2.

Dataset	Unet	LiteResnet
ACDC	0.92 ± 0.02	<b>0.94 ± 0.01*</b>
M&Ms	0.88 ± 0.01	<b>0.90 ± 0.00*</b>
Incor	0.86 ± 0.01	<b>0.87 ± 0.00*</b>
SB	0.90 ± 0.01	<b>0.92 ± 0.01*</b>
LVSC	0.76 ± 0.01	<b>0.81 ± 0.01*</b>
Average	0.86 ± 0.04	<b>0.89 ± 0.04*</b>

\* Statistically significant ( $p < 0.05$  with t-test)

Table 3: Epicardium Dice scores obtained with U-net and LiteResnet tested in set samples from the datasets ACDC, INC, SUN, LVSC, and M&Ms-2

Dataset	Unet	LiteResnet
ACDC	<b>0.96 ± 0.01</b>	0.95 ± 0.01
M&Ms	0.90 ± 0.01	<b>0.93 ± 0.00*</b>
Incor	0.92 ± 0.00	<b>0.93 ± 0.00*</b>
SB	<b>0.93 ± 0.00</b>	<b>0.93 ± 0.00</b>
LVSC	0.81 ± 0.01	<b>0.86 ± 0.01*</b>
Average	0.90 ± 0.04	<b>0.92 ± 0.02*</b>

\* Statistically significant ( $p < 0.05$  with t-test)

Table 4: Myocardium Dice scores obtained with U-net and LiteResnet tested in set samples from the datasets ACDC, INC, SUN, LVSC, and M&Ms-2.

Dataset	Unet	LiteResnet
ACDC	<b>0.89 ± 0.02</b>	<b>0.89 ± 0.02</b>
M&Ms	0.78 ± 0.01	<b>0.81 ± 0.01*</b>
Incor	<b>0.82 ± 0.01</b>	<b>0.82 ± 0.00</b>
SB	<b>0.75 ± 0.01</b>	<b>0.75 ± 0.01</b>
LVSC	<b>0.73 ± 0.01</b>	<b>0.73 ± 0.01</b>
Average	0.79 ± 0.05	<b>0.80 ± 0.05</b>

\* Statistically significant ( $p < 0.05$  with t-test)

As shown in the Tables 2, 3 and 4, the results obtained in datasets previously unseen by the network are similar to those produced in the training datasets' test set for both networks. The average Dice standard deviation across all datasets is relatively low, showing that the networks are fairly generic. The proposed network (LiteResnet) showed an improvement in most of the Dice scores across datasets, the highest

improvement was presented in the LVSC dataset, with the U-net model the achieving a Dice score in the endocardium of 0.76 and with the LiteResnet achieving 0.81, and in the endocardium achieving 0.81 with the U-net and 0.86 with the LiteResnet, indicating that a network with less parameters can perform better in generalizing the learned task.

Although it is difficult to compare our Dice results to those given in the literature because the data utilized differ, we can note that we achieve a better average Dice score in the myocardium in distinct datasets than (PETERSEN, MATTHEWS, *et al.*, 2015).

It's worth noting that various specialists used different labeling approaches to separate the LV in different datasets. Direct comparisons can result in label divergences, which does not necessarily mean that the LV was segmented incorrectly. For example, Figure 28 shows the myocardium delineation presented in one image in the Sunnybrook dataset in the left, and in the right the segmentation performed by the LiteResnet model trained with the ACDC dataset, the Dice between the available mask and the mask learned by the model is 0.58.

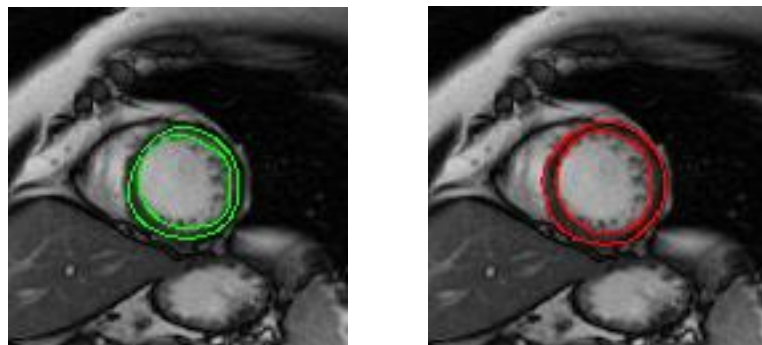


Figure 28: Example of the difference between the ground truth myocardium mask in the Sunnybrook (left) and the segmented by the model trained with the ACDC data (right).

Although the Dice score achieved between the two masks is low, as it can be seen in the images, the network segmented the myocardium correctly, but is not the same as the ground truth mask. Moreover, the myocardium area is very small, so differences in few pixels impacts greatly in the Dice score.

## **5.2. Motion quantification**

The motion estimation result is divided into two groups: (i) indirect form, using the displacement field to warp the myocardium mask; (ii) direct, comparing directly the ground truth from the synthetic data and the displacement learned by the network.

We trained two different network architecture configurations, to explore and compare the performance of each one; we use the PWC and the PWC Siamese. The training performed in both networks consisted of the same hyper-parameters and the dataset used was the ACDC.

In the Table 5 the Dice is displaced between the myocardium mask in the fixed frame and the warped mask in the moving frame, using the displacement field obtained by optical flow method, B-spline registration, PWC, PWC network and the result reported in the literature using the Carmen Network (MORALES, IZQUIERDO-GARCIA, *et al.*, 2019). The methods were applied in three different datasets: ACDC, INC, and Xcat.



Table 5: Dice obtained comparing the fixed myocardium mask and the warped moving myocardium mask using the displacement field generated by different methods (Optical flow, B-spline registration, PWC network, PWC Siamese network and reported in the literature – Carmen) for the ACDC, INC, and Xcat datasets.

	ACDC	INC	Xcat
Optical Flow $\pm$ std	$0.74 \pm 0.07$	$0.76 \pm 0.07$	$0.86 \pm 0.15$
B-Spline $\pm$ std	$0.59 \pm 0.10^*$	$0.58 \pm 0.11^*$	$0.73 \pm 0.15^*$
PWC $\pm$ std	$0.77 \pm 0.04$	$0.74 \pm 0.07$	$0.78 \pm 0.10^*$
PWC Siamese $\pm$ std	<b><math>0.76 \pm 0.06</math></b>	<b><math>0.78 \pm 0.05</math></b>	<b><math>0.85 \pm 0.08</math></b>
Carmen (min-max)	$0.73 (0.68-0.78)^{\#}$	-----	$0.85 (0.81-0.89)^{\#}$

\* Statistically significant ( $p < 0.05$  in the t-test) in comparison with PWC Siamese using the t-test

<sup>#</sup> It is not possible to perform the statistical analysis due to the lack of data

As can be seen in Table 5, the PWC Siamese network performed numerically better than all the other methods in the ACDC dataset, including the result available in the literature. Similarly, PWC Siamese performed numerically better in the INC dataset except for the Carmen network, because the dataset was not included in their work. And in the Xcat dataset, the PWC Siamese result is better than the B-Spline registration, PWC network, and the reported by Morales et al. for the Carmen network. The obtained by PWC Siamese for the Xcat data is similar to the Optical Flow, but with a lower standard deviation.

It is important to highlight that the PWC and PWC Siamese training was performed in the ACDC training set, thus the good results in the INC and Xcat show the generalization of the proposed method.

Because of the lack of displacement ground truth in real images, the direct comparison of the displacement field is done only in the synthetic data. Table 6 shows the results for the mean absolute error, end-point error, and percentage of correct pixel between the Xcat displacement field and the generated by optical flow, B-spline registration, learned by the PWC network, PWC Siamese network, and reported by Morales et al. with the Carmen network.

Table 6: Mean absolute error (MAE), end-point-error (EPE), and percentage of correct pixel (PCP) between the Xcat displacement field and the generated by optical flow technique, B-spline registration, PWC network, PWC Siamese network and reported in the literature (Carmen).

	MAE (pixel)	EPE (pixel)	PCP (%)
Optical Flow $\pm$ std	0.80 $\pm$ 0.43*	1.27 $\pm$ 0.69*	43.94 $\pm$ 10.87*
B-Spline $\pm$ std	1.02 $\pm$ 0.20*	1.62 $\pm$ 0.32*	19.92 $\pm$ 13.61*
PWC $\pm$ std	0.35 $\pm$ 0.14*	0.77 $\pm$ 0.32*	72.12 $\pm$ 12.47*
PWC Siamese $\pm$ std	<b>0.17 <math>\pm</math> 0.10</b>	<b>0.37 <math>\pm</math> 0.23</b>	<b>85.21 <math>\pm</math> 6.71</b>
Carmen (min-max)	-----	1.7 (1.3–2.1) #	-----

\* Statistically significant ( $p < 0.05$  in the t-test) in comparison with PWC Siamese using the t-test

# It is not possible to perform the statistical analysis due to the lack of data

The direct evaluation of the Xcat displacement field and the generated by the automatic methods shows that the PWC Siamese performed better than all the other methods, even when compared with the result available in the literature (Carmen). The good result in the direct evaluation in Table 6, and the good performance shown in Table 5 with an indirect comparison of the displacement field, indicate that it is possible to rely on the indirect form of evaluation in the real images to analyze the performance of the methods.

To illustrate the PWC network performance in predicting the displacement field, in Figure 29 is possible to compare the displacement field generated by the Xcat, in a health simulated subject, and the predicted by the PWC Siamese network, in the x, y, and z directions. The displacement field was set to zero outside of the myocardium mask to ease the visualization. The displacement field is represented here as a color-coded image, where each color represents the amount of movement in each direction. For example, displacement in the x direction in the right part of the myocardium is around -5 mm to -10 mm, and the part in the left is around 2 mm to 5 mm, the x direction negative displacement in the right part of the myocardium and the positive

in the left indicate a contraction, wise because the materials in the boundaries of the myocardium are going towards its center.

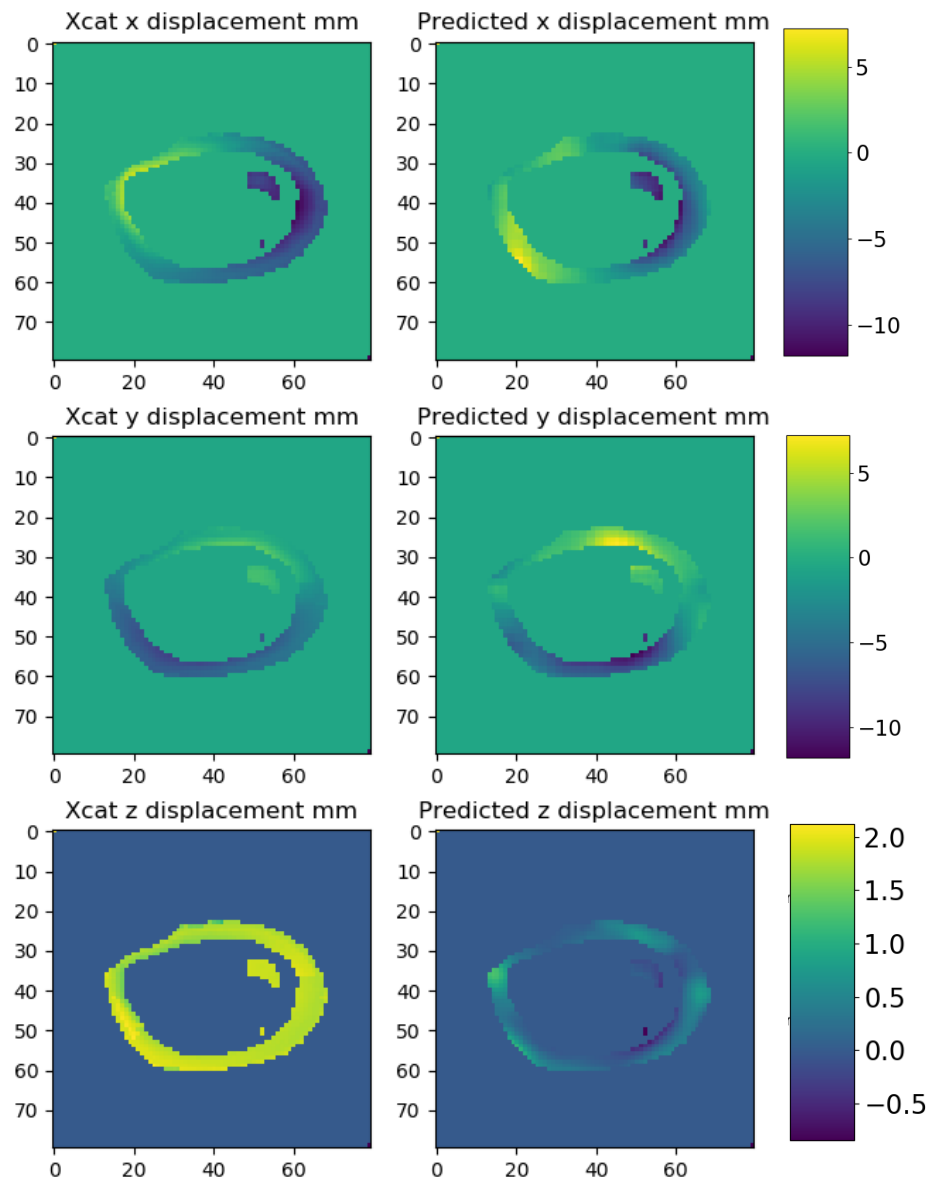


Figure 29: Example of displacement field obtained from a health simulated subject in the Xcat.

All the figures on the left are constructed with data simulated by the Xcat and on the left generated by the PWC Siamese network, in the columns, there are the displacements in the x direction, y direction, and z direction, along with the respective color code representing the amount of movement in that direction. The displacement field outside the myocardium mask was set to zero to ease the visualization.

It is possible to observe in Figure 29 that the z displacement generated by the network is very different from the ground truth (the generated by the Xcat). In general, the

distance between slices in CMR short axis exams is larger than the amount of displacement in the long axis. In the simulated images the distance between slices is 10 mm, and in the example of the image, the displacement in the z direction is around 2 mm. Thus, it is very hard for the network to predict the correct displacement in the z direction with a large slice distance.

### **5.3. Strain**

After generating the displacement field, it is possible to calculate the strain in the three directions of the cardiac orientation: radial, circumferential and longitudinal using equations 7 to 10. With the strain calculated, the polar plot can be constructed for each orientation, described in Figure 18. In the real images used, it is not possible to compare the expected strain with the calculated using the displacement field generated by the network, because of the lack of ground truth. In Figure 30 is possible to perform a qualitative result, comparing the radial strain differences in the myocardium segments for a health subject and a patient with myocardium infarction, both cases belonging to the ACDC dataset. Similarly, Figure 31 and Figure 32 show the differences between health and pathological for the circumferential and longitudinal strain.

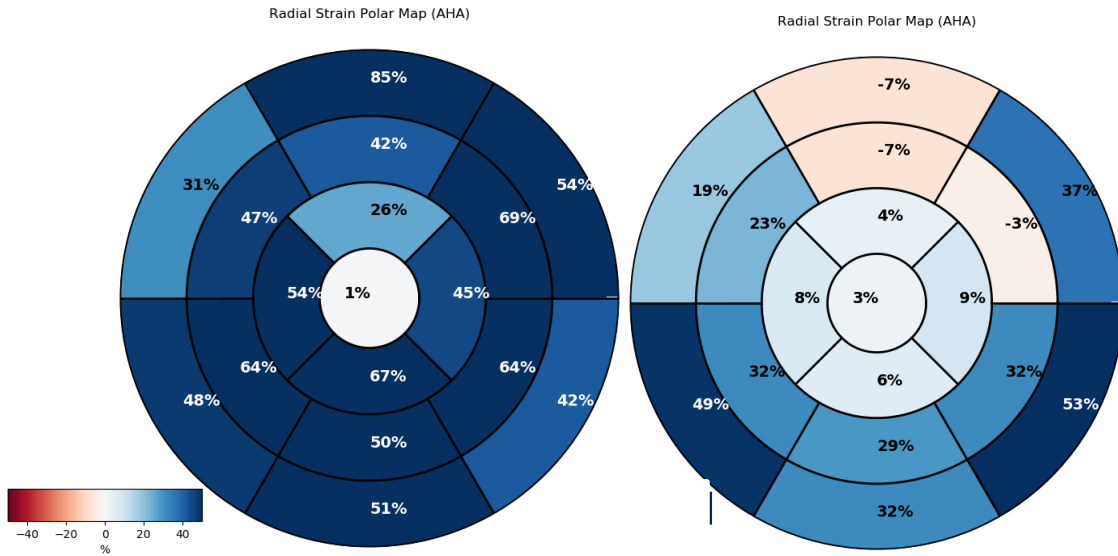


Figure 30: Radial strain calculated with the displacement field learned by the PWC Siamese network for a normal case (left) and a patient with myocardial infarction (right).

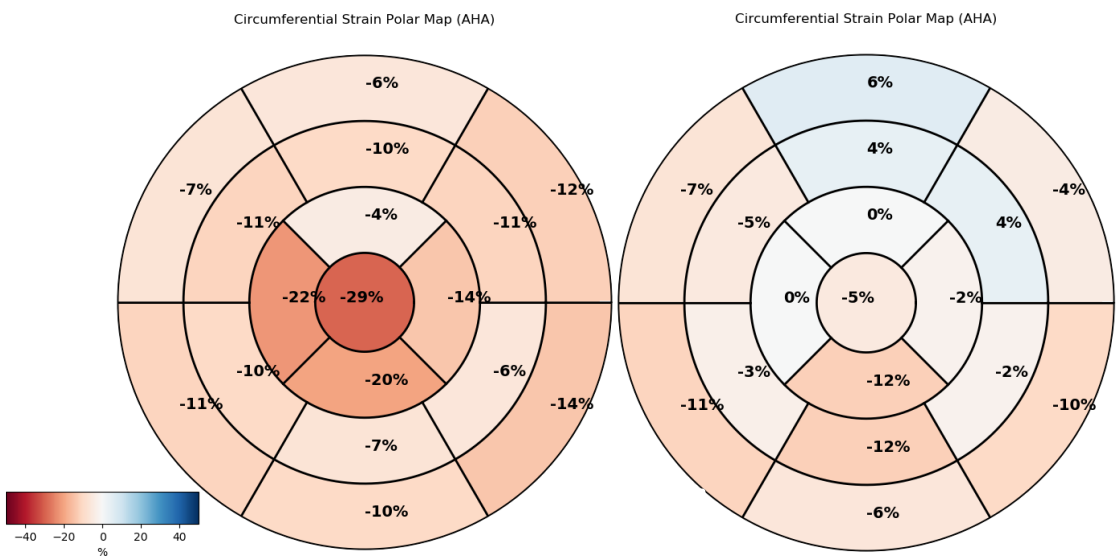


Figure 31: Circumferential strain calculated with the displacement field learned by the PWC Siamese network for a normal case (left) and a patient with myocardial infarction (right).

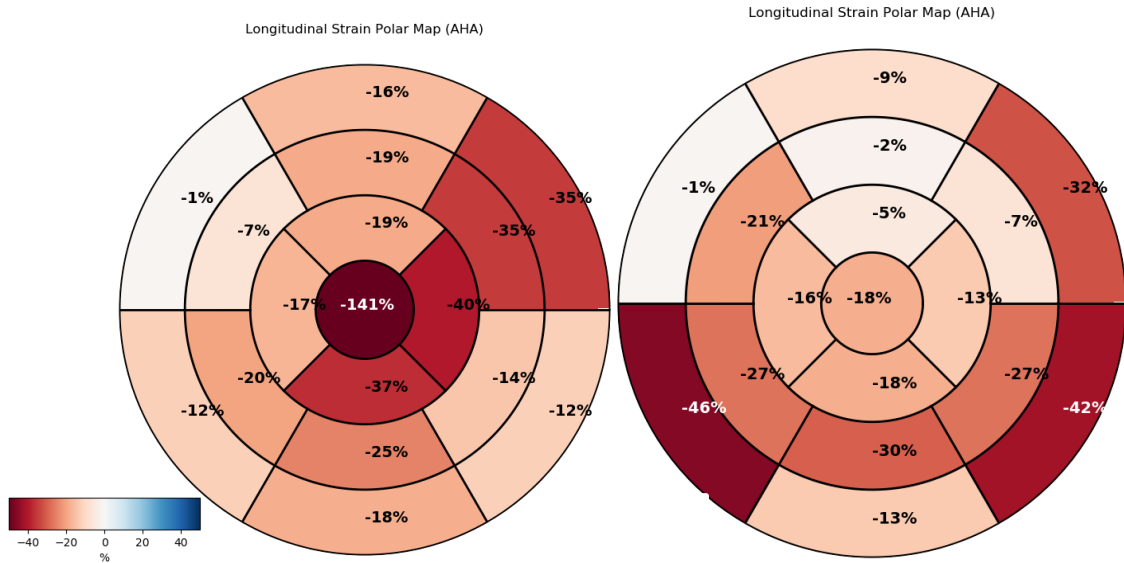


Figure 32: Longitudinal strain calculated with the displacement field learned by the PWC Siamese network for a normal case (left) and a patient with myocardial infarction (right).

According to Amzulescu et al. (2019), there is no consensus in the literature on the definition of strain normal ranges, which makes the quantification of pathological states challenging. The review written by Vo et al. (2018) aimed to estimate a normal range for strain calculated in CMR images using feature tracking methods, the authors detailed that the average values reported by the reviewed papers were 34.1% (28.5% to 39.7%) for global radial strain (GRS), -23% (-24.3% to -21.7%) for global circumferential strain (GCS) and -20.1% (-20.9% to -19.3%) for global longitudinal strain (GLS). In the health case used as an example in the figures 29-31 the GRS calculated is 49.39%, the GCS is -12.02%, and GLS -27.45%.

Due to the large distance between slices in the exams, both of 10 mm, the longitudinal strain values in the segments and the GLS are very different from the expected and reported in the literature. As mentioned before, there is no consensus in the literature about standard values of peak systolic global strain, either radial or circumferential, as reported by Vo et al. (VO, MARWICK, et al., 2018).

Figure 33 and Figure 34 show the reported healthy values of peak systolic strain, respectively, radial and circumferential by some published works as mentioned by Vo et Al. (2018), along with the global strain values obtained by the analyzed methods, the PWC Siamese, Medis and CVI 42 in the 10 healthy subjects. All reported strain was obtained in CMR images.

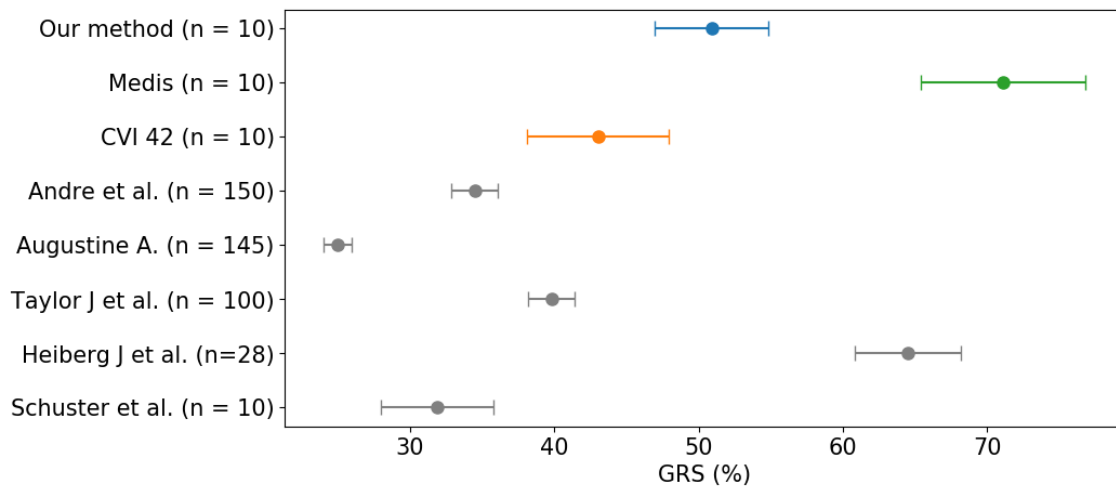


Figure 33: Comparison of the variation of healthy global systolic radial strain obtained by the PWC Siamese method, the Medis and CVI 42, with some values reported in the literature.

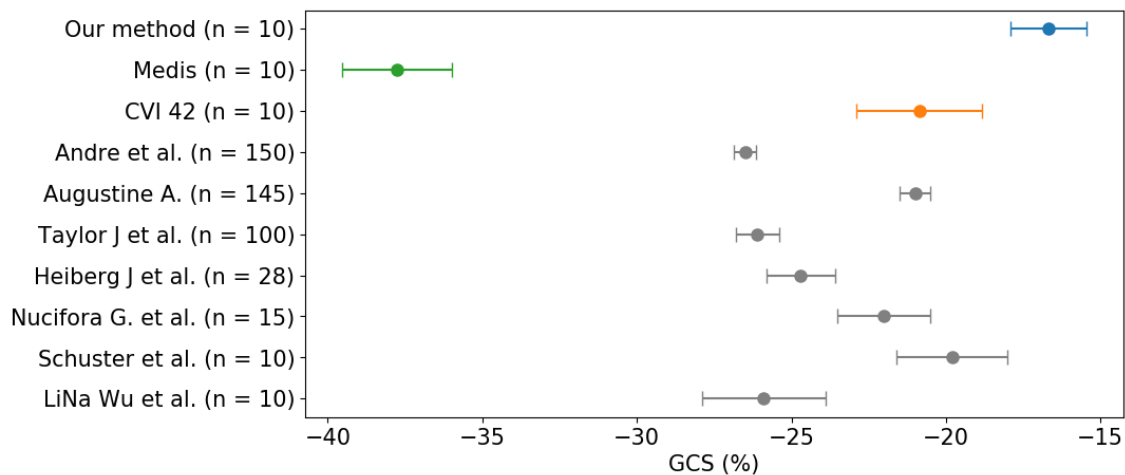


Figure 34: Comparison of the variation of healthy global systolic circumferential strain obtained by the PWC Siamese method, the Medis and CVI 42, with some values reported in the literature.

Without a standard value to compare with, it is difficult to analyze which method is better to determine the strain in comparison to the literature.

The error quantification between the expected strain and the calculated by the proposed method can be executed only in the synthetic data. Table 7 is presented the mean average error (MAE) between the strain calculated using the Xcat displacement field and the generated by different methods, including the classical optical flow and B-spline registration, and the learned by the PWC and PWC Siamese networks. The analysis performed in the synthetic data does not include the commercial systems because those are not suitable for this type of data.

Table 7: Mean absolute error between the calculated strain using the Xcat displacement field and the generated by Optical Flow, B-Spline registration, PWC network, and PWC Siamese network, for each strain direction: radial, circumferential and longitudinal.

	Optical Flow (%)	B-Spline (%)	PWC (%)	PWC Siamese (%)
Radial	2.13 ± 1.33	9.03 ± 3.9	7.55 ± 4.34	12.49 ± 3.77
Circumferential	1.24 ± 0.86	7.77 ± 1.78	6.34 ± 3.23	1.77 ± 1.2
Longitudinal	7.44 ± 5.36	3.28 ± 2.3	5.22 ± 2.71	3.63 ± 3.03

As can be observed in Table 7, the Optical Flow method presented the lowest MAE and standard deviation in the radial and circumferential, and the other methods also resulted in lower MAE than the PWC Siamese. However, in some cases the strain resulted is very small, then, the difference between small ground truth strains compared with a small strain generated by the methods results in a small error.

Figure 35, 35 and 36 show the box-plot of the calculated radial, circumferential and longitudinal strain, respectively, using the motion field from the different analyzed methods, alongside the ground truth. In the box plot, the simulated exams are divided into three ejection fraction categories: normal, lower function and heart failure, to better investigate the strain distribution in different scenarios.



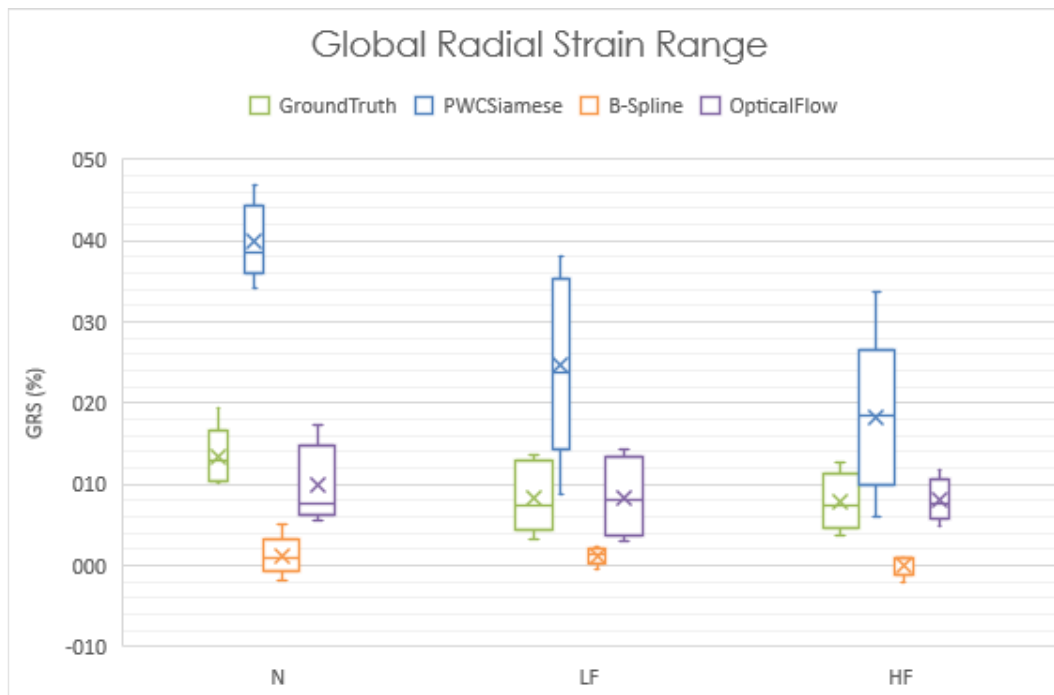


Figure 35: Box-plot of the global radial strain (GRS) calculated using the motion field from de ground truth XCAT and from the PWC Siamese, the B-Spline registration and the optical flow. Exams are divided into three ejection fraction categories: normal (N), lower function (LF) and heart failure (HF).

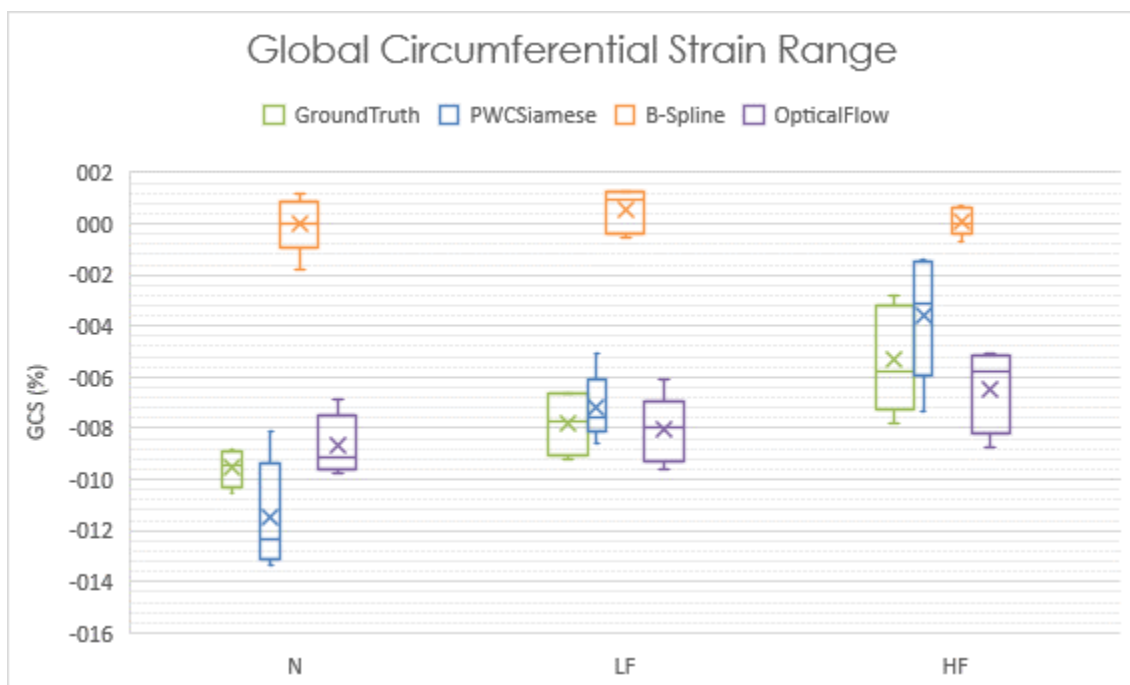


Figure 36: Box-plot of the global circumferential strain (GCS) calculated using the motion field from de ground truth XCAT and from the PWC Siamese, the B-Spline registration and the optical flow. Exams are divided into three ejection fraction categories: normal (N), lower function (LF) and heart failure (HF).

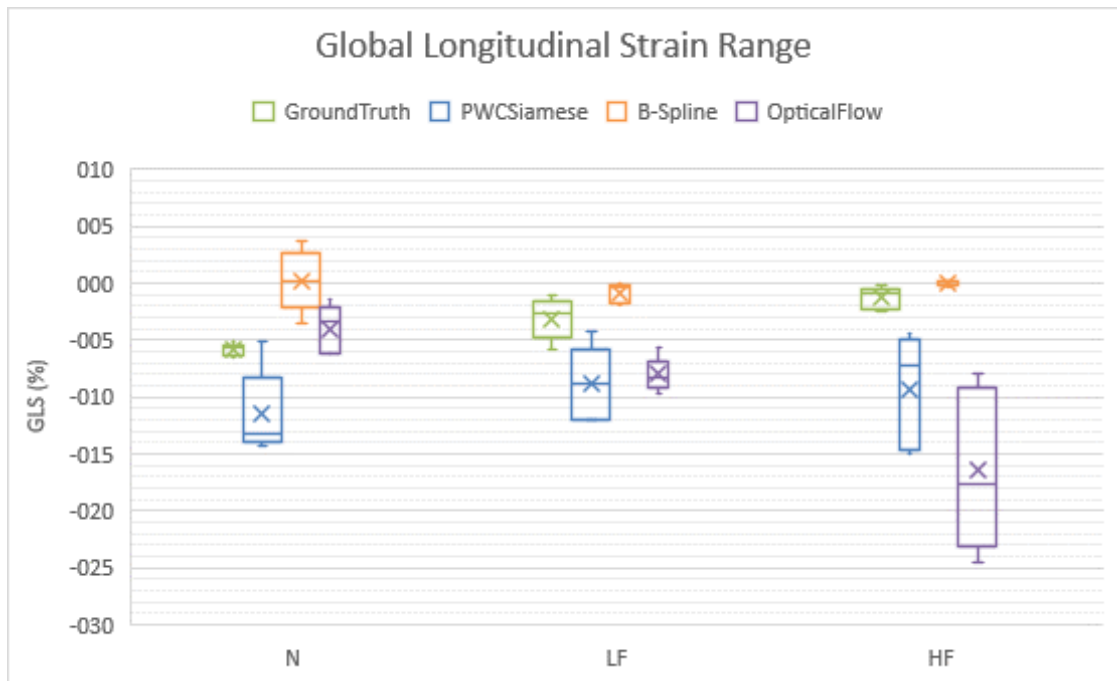


Figure 37 Box-plot of the global longitudinal strain (GLS) calculated using the motion field from de ground truth XCAT and from the PWC Siamese, the B-Spline registration and the optical flow. Exams are divided into three ejection fraction categories: normal (N), lower function (LF) and heart failure (HF).

As can be observed in the Figures above, the range of strain values calculated using the B-spline registration is too close to zero, and it reflects in the MAE in Table 7. There were no differences between the various groups in the average global strain in the radial direction determined by optical flow.

To analyze the strain quantification in the real CMR images, the wall motion score classification performed by the professional was compared with the strain generated by the automatic quantification using the PWC Siamese, and the commercial software available in the market: CVI 42 and Medis, along with the strain calculated using the optical flow and B-spline registration methods. A box plot (Figure 38) was constructed to compare the WMS class and the strain obtained by the different methods.

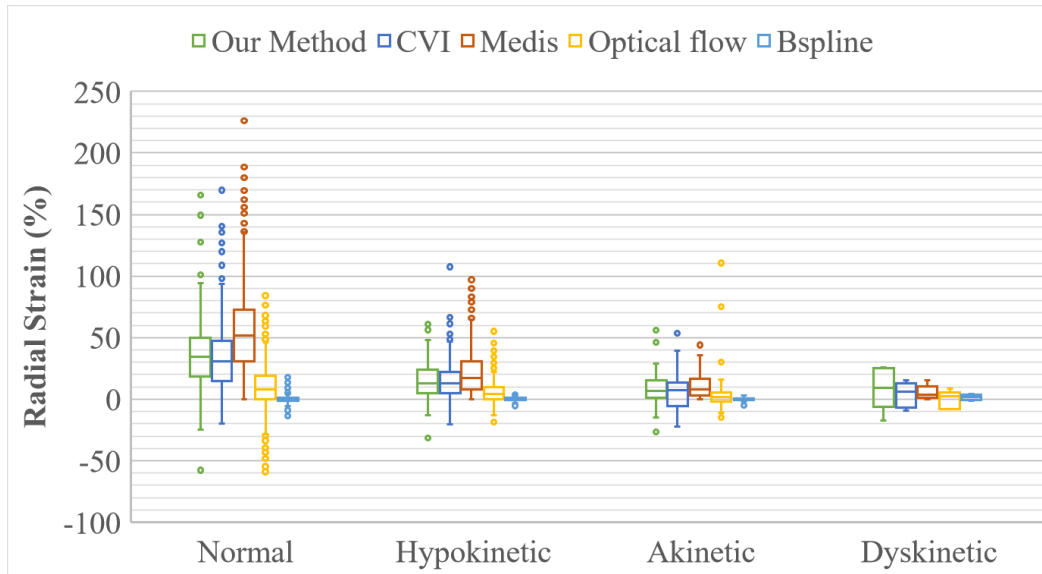


Figure 38: Box plot comparing WMS class distribution with strain values obtained by the CVI 42, Medis, and strain quantification using the PWC Siamese networks (our method), optical flow and Bspline displacement fields.

As it can be seen in Figure 38 the proposed method follows a linear tendency for the strain values and WMS classes, along with the other methods. The classical methods, optical flow and Bspline presented displacement very close to zero, consequently, the calculate strain is very small for all the WMS classes, as it can be seen in the Figure 38.

One important ability of a strain quantification system is to distinguish between healthy and unhealthy subjects, related to cardiomyopathy that affects the cardiac deformation. To compare our automated technique to commercial solutions, we created a box plot (see Figure 39) that shows the distribution of global strain in healthy (NOR) and non-healthy (NOT NOR) groups. As previously stated, the dataset employed in the strain evaluation consists of 10 healthy control participants and 52 patients with various heart diseases.

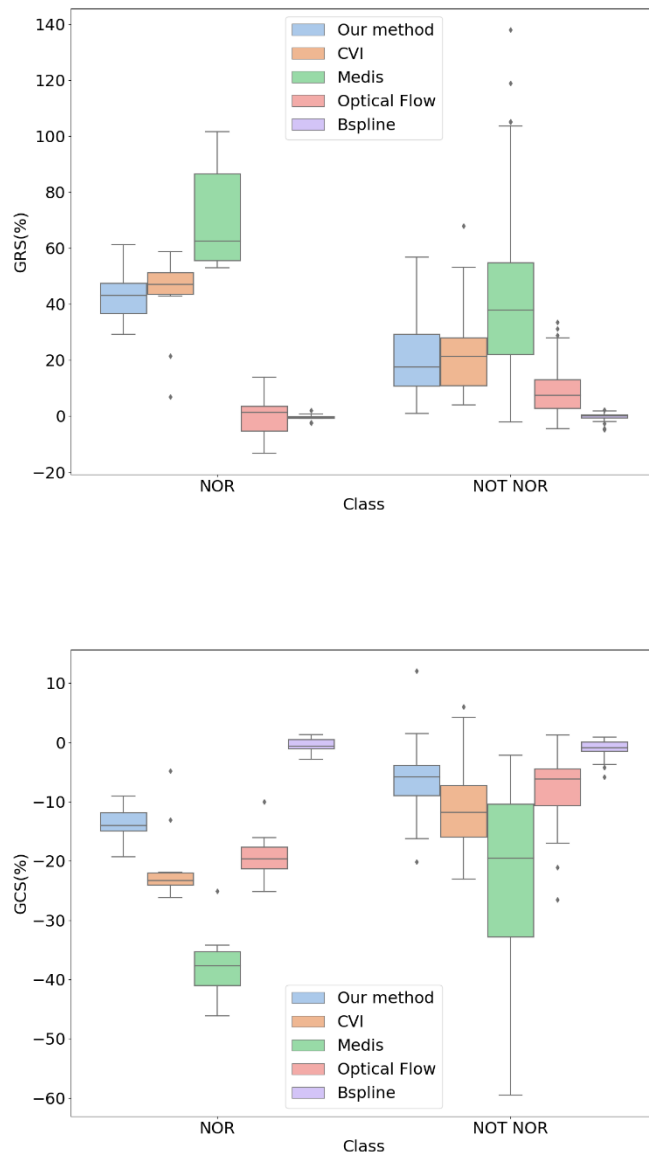


Figure 39: (up) Global radial strain (GRS) and (bottom) global circumferential strain (GCS) for all the strain quantification methods Medis, CVI, our method, optical flow and Bspline for each group of subjects: normal (NOR) and not normal (NOT NOR).

In the healthy group (NOR), the standard deviation of the GRS achieved by the proposed technique is lower than that obtained by the Medis systems. The smaller strain variance in healthy people shows that the proposed technique is superior to the one available in the marketing, to determine peak systolic global strain.

To better analyze the potential of the proposed method compared to the two commercially available methods and the classical methods, a logistic regression classification system between normal and not normal (other classes) was performed using the radial and circumferential strain data. Cross fold validation, using 4 folds, was applied in the analysis to estimate the classification performance in different selected data. The Receiver Operating Characteristic Curve (ROC curve) for the classification system for each method was elaborated, using 4-fold cross-validation, Figure 40 shows the ROC curve for the PWC Siamese derived radial strain (our method), CVI 42 data, and Medis data, optical flow and bspline calculated strain, and Figure 41 shows de ROC curve for the classification system build using the circumferential strain data.

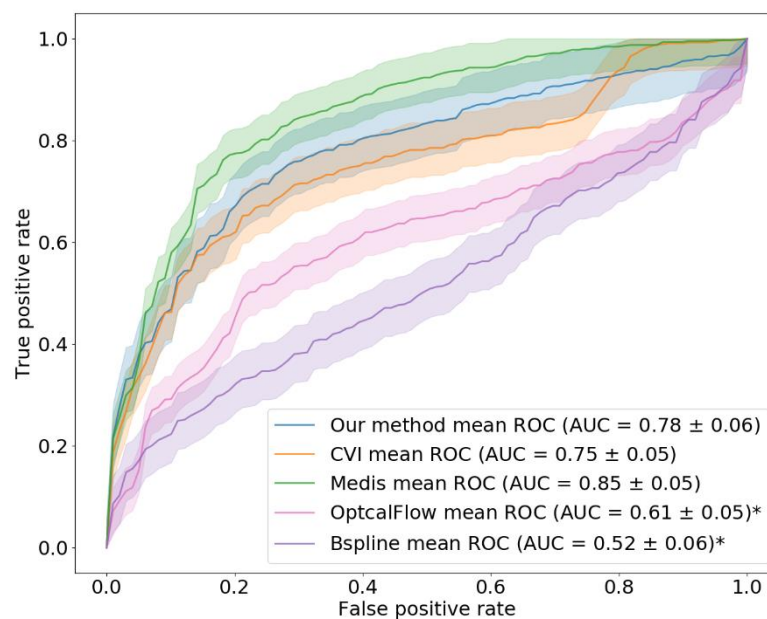


Figure 40: ROC curve for the classification system using logistic regression to classify normal and not normal WMS classes using radial strain data from our method, CVI 42 system, Medis system, optical flow and bspline method, using 4-folds cross-validation.

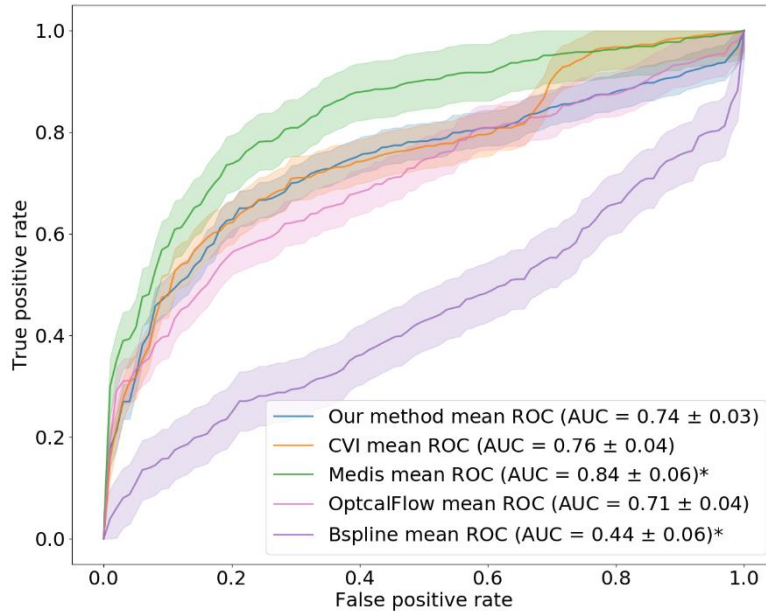


Figure 41: ROC curve for the classification system using logistic regression to classify normal and not normal WMS classes using circumferential strain data from our method, CVI 42 system, Medis system, optical flow and bspline method, using 4-folds cross-validation.

As observed in Figure 40, the classification system build with the PWC Siamese data shows an AUC similar to the CVI 42 and Medis, to classify the myocardium regions into normal motion and not normal, according to the clinical classification performed by a professional. In comparison with the Medis classification system, the PWC presented a worse AUC in the circumferential data. The classification systems using the classical methods (optical flow and Bspline) presented worse performance than all the other methods.

Although the myocardium motion classification into normal and not normal, according to the circumferential strain, of the proposed method showed worse performance than the Medis, our deep learning-based automatic method operates independently of human observers, making it user-agnostic and invariant to user variations.

One radiologist replicates the strain analysis in the same software twice for 20 exams, to examine the intra-observer variance. Also, two different radiologists performed the strain analyses in the commercial systems for the same 20 exams, to investigate the inter-observer variation. Table 8 shows the MAE obtained in the intra- and inter-observer analysis for the CVI 42 and Medis.

Table 8: MAE for the CVI 42 and Medis intra- and inter-observer analyses.

Analysis	Radial (%)		Circumferential (%)	
	Intra	Inter	Intra	Inter
Medis	20.07 ± 21.16	23.97 ± 24.45	3.76 ± 4.26	4.87 ± 4.75
CVI 42	22.26 ± 24.13	20.53 ± 17.62	11.35 ± 11.39	9.66 ± 8.18

Figure 42 and Figure 43 show, respectively, the regional radial and circumferential strain Bland-Altman plot for the intra-observer analysis in both commercial systems, CVI 42 and Medis.

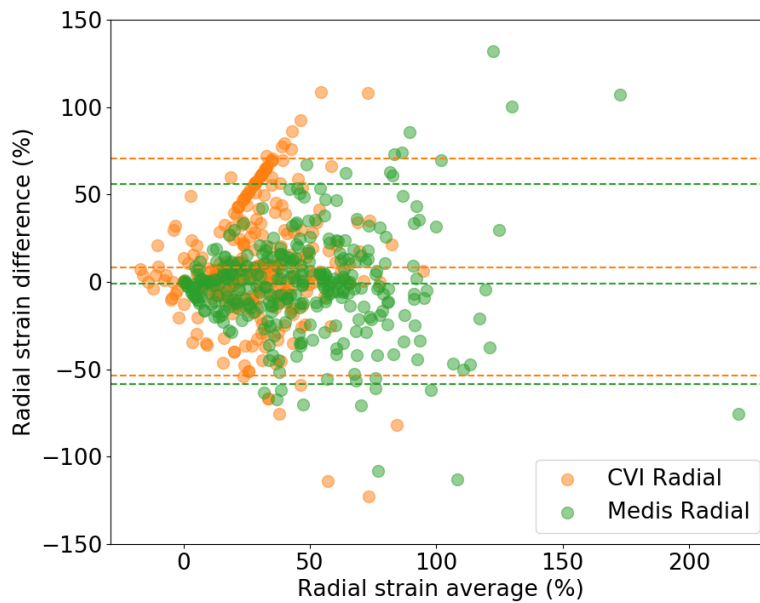


Figure 42: Bland-Altman plot for the intra-observer radial local strain in the CVI 42 system (orange) and Medis System (green).

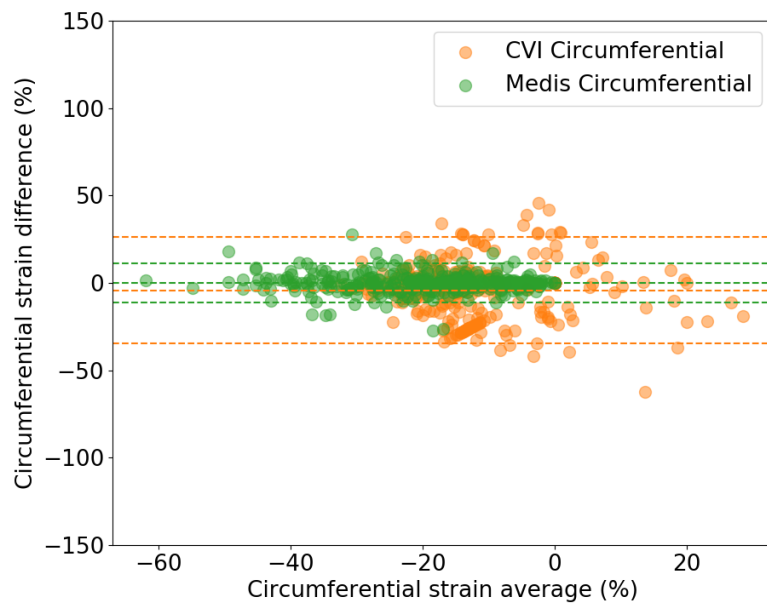


Figure 43: Bland-Altman plot for the intra-observer circumferential local strain in the CVI 42 system (orange) and Medis System (green).

In Figure 44 is the Bland-Altman plot for the inter-observer analysis in the CVI 42 and Medis systems, and in Figure 45 is the Bland-Altman plot for the circumferential strain inter-observer variation.

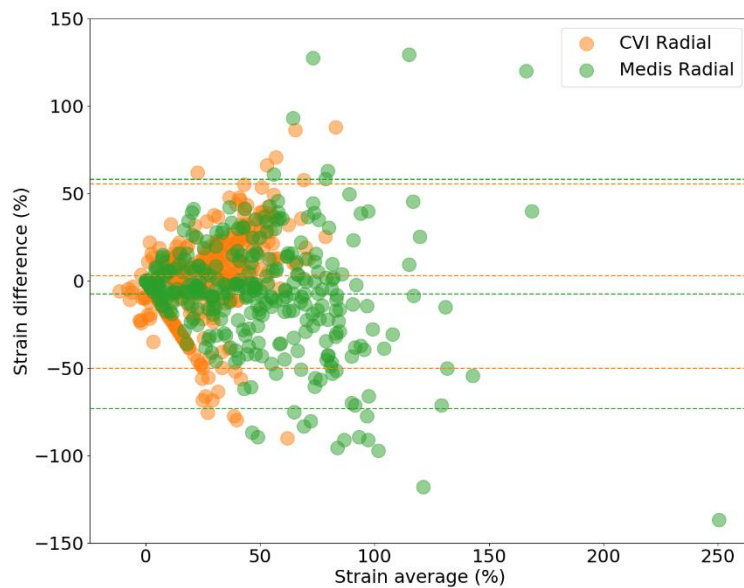


Figure 44: Bland-Altman plot for the inter-observer analysis with radial local strain, performed with the Medis (green) and CVI 42 (orange) data.



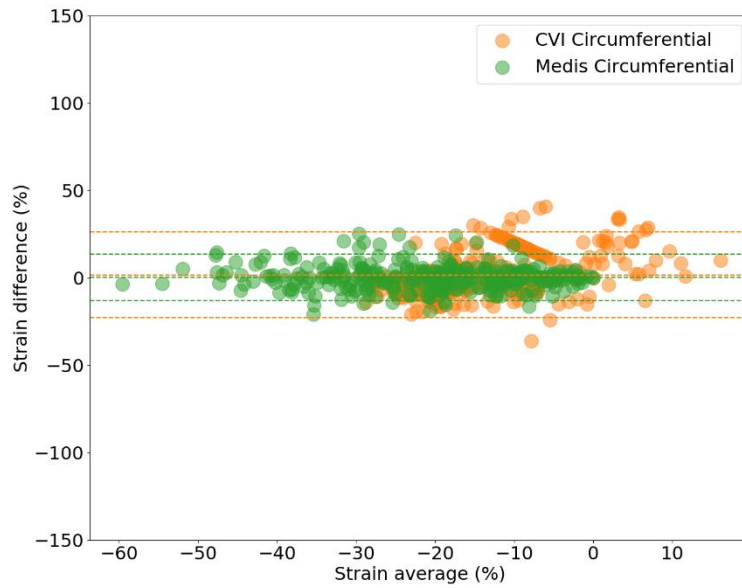


Figure 45: Bland-Altman plot for the inter-observer analysis with circumferential local strain, performed with the Medis (green) and CVI 42 (orange) data.

According to Figure 42 and Figure 43, it is possible to observe that the circumferential strain suffers less divergence in the intra-analyses compared with the radial, in both systems. It may happen due to the range of values in both directions, during the myocardium contraction the degree of motion in the radial direction is much higher than in the circumferential, resulting that absolute values in the radial strain being higher than in the circumferential, and consequently, the range of error is higher too. The inter-observer analyses follow almost the same behavior as the inter-observer, suggesting that the disparity of value is related not only with a different observer, but the values diverge with the analysis, even with the same observer. That difference in values according to the analysis reduces the reproducibility of the commercial systems.

The proposed automatic strain quantification method using deep learning is invariant to the observer, since the method does not require any user interaction, differently

from the commercial software CVI 42 and Medis. Therefore, using deep learning to quantify strain in cardiac resonance images seems to be a more reliable source to understand cardiac diseases than the available methods.

As mentioned before, Morales et al. (2021) developed an automatic pipeline to estimate cardiac strain in CMR images using deep learning, which they called the solution DeepStrain. However, they did not explore generalization to other public datasets and one of the tests was performed on the same dataset of training.

To compare our solution with DeepStrain, the source code provided by Morales et al. was used to test the pipelines in a public dataset unseen by both methods, the M&Ms-2 (CAMPELLO, GKONTRA, *et al.*, 2021). There is any quantitative metric available to compare both systems. To evaluate the performances, a graph with the global radial strain (GRS) through the cardiac cycle was built with the result of both pipelines, presented in Figure 46. In the GRS curves, the subjects' normal health and not normal was separated, and a qualitative evaluation can be performed by analyzing how much each system separates the healthy and non-healthy groups.

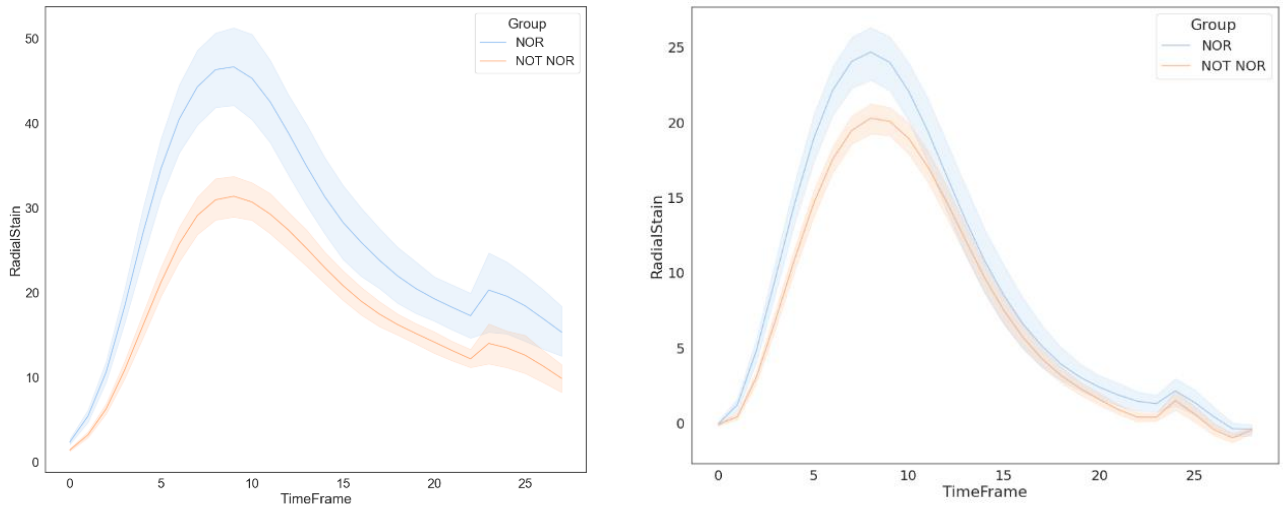


Figure 46: Global radial strain over the cardiac cycle resulted by the application of our pipeline (left) and the DeepStrain (right) in the M&Ms-2 dataset, showing the curves for the normal group (NOR) and not normal (NOT NOR).

Because databases lack true strain labels, we may compare our method to those described in the literature indirectly, which makes quantitative comparison of methods challenging. When analyzing the graphs in Figure 46, it can be seen that our approach yields a bigger gap between the curves of the normal and non-normal classes, implying that our method performs better. It is important to note that the evaluation was conducted using a dataset that neither approach had before faced, implying that our solution generalized better than Morales et al.'s (MORALES, VAN DEN BOOMEN, *et al.*, 2021).

Furthermore, we conducted a comparative analysis of both methods, one proposed in our study and the other introduced by Morales, with a focus on assessing the complexity of the models. Table 9 presents the number of parameters and the average inference time for a single exam in the LiteResnet and CarSon models, which are utilized for cardiac structure segmentation in our research and in Morales' work, respectively. Additionally, Table 9 provides details on the parameters and inference

time for the motion estimation models introduced in our research (PWC Siamese) and those presented in Morales' publication (CarMen). The inference time measurements were obtained using an NVIDIA Tesla v100 16GB GPU.

Table 9: Number of trainable parameters and average inference time of the models, including the segmentation models and the motion estimation models.

	Model	Parameters (millions)	Inference time (s)
Segment.	LiteResnet	0.58	0.03
	CarSon	57.2	13.5
Motion	PWC Siamese	10.5	3.6
	CarMen	111.8	8.5

Comparing our study's models to Morales', we find that they are less complex and handle data more quickly. The PWC Siamese model is 10 times less in terms of parameters than CarMen, and our motion model's average inference time is 2.4 times faster than that suggested by Morales, as seen in Table 9.

## 6. CONCLUSION

In this work, a novel approach based on DL to measure myocardial strain in CMR with 2D-SSFP pulse sequence was developed and assessed. We established a hybrid pipeline that employs both supervised and unsupervised DL to automatically perform the tasks necessary for cardiac muscle segmentation and motion estimation. We investigated the generalizability of a supervised DL segmentation method to define the heart muscle, and the use of an unsupervised DL model to track motion within the left ventricle in both real and synthetic 3D cine magnetic resonance images. Finally, we looked into the connection between the segmented myocardium and the estimated motion to calculate myocardial strain.

The results of this research demonstrated the potential of deep learning techniques in automating processes and enhancing the accuracy of myocardial strain quantification. The proposed pipeline showed promising results in the strain estimation, achieving AUC of 0.78 for classifying the WMS normal class using the radial strain values calculated by the proposed method. Additionally, the proposed method exhibits exceptional accuracy in segmenting the cardiac muscle, obtaining an average myocardium Dice score of 0.80 when tested across five distinct datasets. Moreover, the proposed approach demonstrated strong performance in tracking cardiac motion, with an EPE of just 0.37 pixels when applied to synthetic data. The promising results from the automated method have the potential to significantly assist in the diagnosis and monitoring of cardiac diseases. Furthermore, the incorporation of deep learning techniques into the segmentation and motion estimation processes streamlines the workflow, reducing the necessity for manual intervention, consequently saving time and enhancing the overall efficiency.

In conclusion, this research highlights the potential of deep learning in improving the accuracy and efficiency of cardiac imaging analysis. The presented approach holds substantial clinical implications, offering clinicians valuable insights into cardiac function and disease diagnosis. The study establishes that deep learning techniques can be employed to accurately quantify myocardial strain, and this methodology could potentially extend to other modalities of medical imaging, ultimately leading to improved patient outcomes.

## **7. PUBLISHED ARTICLES**

DE VITA GRAVES, C.; REBELO, M. F. S.; MORENO, R. A.; NOMURA, C.  
H.; GUTIERREZ, M. A.; V. GRAVES, C.; REBELO, M. F. S.; MORENO, R. A.;

DANTAS-JR, R. N.; ASSUNÇÃO-JR, A. N.; NOMURA, C. H.; GUTIERREZ, M. A.; DE VITA GRAVES, C.; REBELO, M. F. S.; MORENO, R. A.; NOMURA, C. H.; GUTIERREZ, M. A. Siamese Pyramidal Deep Learning Network for Strain Estimation in 3D Cardiac Cine-MR. *Computerized Medical Imaging and Graphics*, vol. 108, p. 102283, Aug. 2023. DOI 10.1016/j.compmedimag.2023.102283. Available at: <https://linkinghub.elsevier.com/retrieve/pii/S0895611123001015>.

GRAVES, C. V., REBELO, M. F. S., MORENO, R. A., et al. "Automatic myocardium strain quantification in MR synthetic images with Deep Learning". 11 jul. 2022. *Anais [...] [S.l.]*, IEEE, 11 jul. 2022. p. 545–548. DOI: 10.1109/EMBC48229.2022.9871516. Available at: <https://ieeexplore.ieee.org/document/9871516/>.

GRAVES, C. V., MORENO, R. A., REBELO, M. F. S., et al. "Cardiac motion estimation using pyramid, warping, and cost volume neural network". 15 fev. 2021. *Anais [...] [S.l.]*, SPIE, 15 fev. 2021. p. 30. DOI: 10.1117/12.2582180. Available at: <https://www.spiedigitallibrary.org/conference-proceedings-of-spie/11600/2582180/Cardiac-motion-estimation-using-pyramid-warping-and-cost-volume-neural/10.1117/12.2582180.full>.

GRAVES, C. V., MORENO, R. A., REBELO, M. S., et al. "Improving the generalization of deep learning methods to segment the left ventricle in short axis MR images". jul. 2020. *proceedings [...] [S.l.]*, IEEE, jul. 2020. p. 1203–1206. DOI: 10.1109/EMBC44109.2020.9175256. Available at: <https://ieeexplore.ieee.org/document/9175256/>.

## 8. BIBLIOGRAPHY

ABDELTAWAB, H., KHALIFA, F., TAHER, F., *et al.* "A deep learning-based approach for automatic segmentation and quantification of the left ventricle from cardiac cine MR images", **Computerized Medical Imaging and Graphics**, v. 81, p. 101717, abr. 2020.

DOI: 10.1016/j.compmedimag.2020.101717. Disponível em:  
<https://linkinghub.elsevier.com/retrieve/pii/S0895611120300203>.

AHMADI, A., PATRAS, I. "Unsupervised convolutional neural networks for motion estimation". 2016. **Anais [...]** [S.l.: s.n.], 2016. DOI: 10.1109/ICIP.2016.7532634.

AMZULESCU, M. S., DE CRAENE, M., LANGET, H., *et al.* "Myocardial strain imaging: review of general principles, validation, and sources of discrepancies", **European Heart Journal - Cardiovascular Imaging**, v. 20, n. 6, p. 605–619, 1 jun. 2019.

DOI: 10.1093/ehjci/jez041. Disponível em:  
<https://academic.oup.com/ehjcmimaging/article/20/6/605/5418560>.

AVENDI, M. R., KHERADVAR, A., JAFARKHANI, H. "A combined deep-learning and deformable-model approach to fully automatic segmentation of the left ventricle in cardiac MRI", **Medical Image Analysis**, v. 30, p. 108–119, 2016. DOI:

10.1016/j.media.2016.01.005. Disponível em:  
<http://dx.doi.org/10.1016/j.media.2016.01.005>.

BAI, W., SINCLAIR, M., TARRONI, G., *et al.* "Automated cardiovascular magnetic resonance image analysis with fully convolutional networks", **Journal of Cardiovascular Magnetic Resonance**, v. 20, n. 1, p. 65, 14 dez. 2018. DOI:

10.1186/s12968-018-0471-x. Disponível em: <https://jcmr->

online.biomedcentral.com/articles/10.1186/s12968-018-0471-x.

BERNARD, O., LALANDE, A., ZOTTI, C., *et al.* "Deep Learning Techniques for Automatic MRI Cardiac Multi-Structures Segmentation and Diagnosis: Is the Problem Solved?", **IEEE Transactions on Medical Imaging**, v. 37, n. 11, p. 2514–2525, nov. 2018. DOI: 10.1109/TMI.2018.2837502. Disponível em: <https://ieeexplore.ieee.org/document/8360453/>.

BHUVA, A. N., BAI, W., LAU, C., *et al.* "A Multicenter, Scan-Rescan, Human and Machine Learning CMR Study to Test Generalizability and Precision in Imaging Biomarker Analysis", **Circulation: Cardiovascular Imaging**, v. 12, n. 10, p. 1–11, out. 2019. DOI: 10.1161/CIRCIMAGING.119.009214. Disponível em: <https://www.ahajournals.org/doi/10.1161/CIRCIMAGING.119.009214>.

CAMPELLO, V. M., GKONTRA, P., IZQUIERDO, C., *et al.* "Multi-Centre, Multi-Vendor and Multi-Disease Cardiac Segmentation: The M&Ms Challenge", **IEEE Transactions on Medical Imaging**, v. 40, n. 12, p. 3543–3554, dez. 2021. DOI: 10.1109/TMI.2021.3090082. Disponível em: <https://ieeexplore.ieee.org/document/9458279/>.

CERQUEIRA, M. D., WEISSMAN, N. J., DILSIZIAN, V., *et al.* "Standardized Myocardial Segmentation and Nomenclature for Tomographic Imaging of the Heart", **Journal of Cardiovascular Magnetic Resonance**, v. 105, n. 4, p. 539–542, 29 jan. 2002. DOI: 10.1081/JCMR-120003946. Disponível em: <https://www.ahajournals.org/doi/10.1161/hc0402.102975>.

CHEN, C., BAI, W., DAVIES, R. H., *et al.* "Improving the Generalizability of Convolutional Neural Network-Based Segmentation on CMR Images", **Frontiers in Cardiovascular Medicine**, v. 7, n. June, p. 1–17, 2020. DOI: 10.3389/fcvm.2020.00105.



Disponível em: <http://arxiv.org/abs/1907.01268>.

CHEN, C., QIN, C., QIU, H., *et al.* "Deep Learning for Cardiac Image Segmentation: A Review", **Frontiers in Cardiovascular Medicine**, 2020. DOI: 10.3389/fcvm.2020.00025. .

COLLETTI, P. M. **Multicenter, Scan-Rescan, Human and Machine Learning CMR Study to Test Generalizability and Precision in Imaging Biomarker Analysis: A Solid Basis for Future Work. Circulation: Cardiovascular Imaging.** [S.l: s.n.]. Disponível em: <https://www.ahajournals.org/doi/10.1161/CIRCIMAGING.119.009759>. , out. 2019

CURIALE, A. H., BERNARDO, A., CÁRDENAS, R., *et al.* "CardIAc: an open-source application for myocardial strain analysis", **International Journal of Computer Assisted Radiology and Surgery**, v. 16, n. 1, p. 65–79, 16 jan. 2021. DOI: 10.1007/s11548-020-02291-z. Disponível em: <http://link.springer.com/10.1007/s11548-020-02291-z>.

D'HOOGE, J. "Regional Strain and Strain Rate Measurements by Cardiac Ultrasound: Principles, Implementation and Limitations", **European Journal of Echocardiography**, v. 1, n. 3, p. 154–170, set. 2000. DOI: 10.1053/euje.2000.0031. Disponível em: <https://academic.oup.com/ehjcmimaging/article-lookup/doi/10.1053/euje.2000.0031>.

DARTON, N. J., IONESCU, A., LLANDRO, J. **Magnetic nanoparticles in biosensing and medicine.** [S.l: s.n.], 2019.

DOSOVITSKIY, A., FISCHER, P., ILG, E., *et al.* "FlowNet: Learning Optical Flow with Convolutional Networks". dez. 2015. **Anais [...]** [S.l.], IEEE, dez. 2015. p. 2758–2766. DOI: 10.1109/ICCV.2015.316. Disponível em: <https://ieeexplore.ieee.org/document/7410673/>.

DUCHATEAU, N., KING, A. P., DE CRAENE, M. "Machine Learning Approaches for Myocardial Motion and Deformation Analysis", **Frontiers in Cardiovascular Medicine**, v. 6, n. January, p. 1–9, 9 jan. 2020. DOI: 10.3389/fcvm.2019.00190. Disponível em: <https://www.frontiersin.org/article/10.3389/fcvm.2019.00190/full>.

EPSTEIN, F. "MRI of left ventricular function", **Journal of Nuclear Cardiology**, v. 14, n. 5, p. 729–744, set. 2007. DOI: 10.1016/j.nuclcard.2007.07.006. Disponível em: <http://link.springer.com/10.1016/j.nuclcard.2007.07.006>.

FERDIAN, E., SUINESIAPUTRA, A., FUNG, K., *et al.* "Fully Automated Myocardial Strain Estimation from Cardiovascular MRI-tagged Images Using a Deep Learning Framework in the UK Biobank", **Radiology: Cardiothoracic Imaging**, v. 2, n. 1, p. e190032, 1 fev. 2020. DOI: 10.1148/ryct.2020190032. Disponível em: <http://pubs.rsna.org/doi/10.1148/ryct.2020190032>.

GOODFELLOW, I., BENGIO, Y., COURVILLE, A. **Deep Learning**. [S.l.], MIT Press, 2016. Disponível em: <http://www.deeplearningbook.org>.

GRAVES, C. V., MORENO, R. A., REBELO, M. F. S., *et al.* "Cardiac motion estimation using pyramid, warping, and cost volume neural network", **Medical Imaging 2021: Biomedical Applications in Molecular, Structural, and Functional Imaging**, n. February 2021, p. 30, 15 fev. 2021. DOI: 10.1117/12.2582180. Disponível em: <https://www.spiedigitallibrary.org/conference-proceedings-of-spie/11600/2582180/Cardiac-motion-estimation-using-pyramid-warping-and-cost-volume-neural/10.1117/12.2582180.full>.

GRAVES, C. V., MORENO, R. A., REBELO, M. S., *et al.* "Improving the generalization of deep learning methods to segment the left ventricle in short axis MR images", **Proceedings of the Annual International Conference of the IEEE Engineering in**

**Medicine and Biology Society, EMBS**, v. 2020- July, p. 1203–1206, jul. 2020. DOI: 10.1109/EMBC44109.2020.9175256. Disponível em:

<https://ieeexplore.ieee.org/document/9175256/>.

HALL, J. E., GUYTON, A. C. **Tratado de Fisiologia Médica**. 12. ed. Rio de Janeiro, Elsevier, 2011.

HAYKIN, S. **Neural Networks and Learning Machines**. [S.l: s.n.], 2008. v. 3.

HE, K., ZHANG, X., REN, S., *et al.* "Deep Residual Learning for Image Recognition". jun. 2016. **Anais** [...] [S.l.], IEEE, jun. 2016. p. 770–778. DOI: 10.1109/CVPR.2016.90. Disponível em: <http://ieeexplore.ieee.org/document/7780459/>.

HUANG, Z., SHI, X., ZHANG, C., *et al.*, "FlowFormer: A Transformer Architecture for Optical Flow". [S.l: s.n.], 2022. p. 668–685. DOI: 10.1007/978-3-031-19790-1\_40. Disponível em: [https://link.springer.com/10.1007/978-3-031-19790-1\\_40](https://link.springer.com/10.1007/978-3-031-19790-1_40).

HUI WANG, AMINI, A. A. "Cardiac Motion and Deformation Recovery From MRI: A Review", **IEEE Transactions on Medical Imaging**, v. 31, n. 2, p. 487–503, fev. 2012. DOI: 10.1109/TMI.2011.2171706. Disponível em: <http://ieeexplore.ieee.org/document/6044719/>.

ILG, E., MAYER, N., SAIKIA, T., *et al.* "FlowNet 2.0: Evolution of Optical Flow Estimation with Deep Networks". 2017-Janua, jul. 2017. **Anais** [...] [S.l.], IEEE, jul. 2017. p. 1647–1655. DOI: 10.1109/CVPR.2017.179. Disponível em: <http://ieeexplore.ieee.org/document/8099662/>.

KHENED, M., KOLLERATHU, V. A., KRISHNAMURTHI, G. "Fully convolutional multi-scale residual DenseNets for cardiac segmentation and automated cardiac diagnosis using ensemble of classifiers", **Medical Image Analysis**, v. 51, p. 21–45, jan. 2019. DOI: 10.1016/j.media.2018.10.004. Disponível em:

<https://linkinghub.elsevier.com/retrieve/pii/S136184151830848X>.

KRAMER, C. M. "Role of Cardiac MR Imaging in Cardiomyopathies", **Journal of Nuclear Medicine**, v. 56, n. Supplement\_4, p. 39S-45S, 1 jun. 2015. DOI: 10.2967/jnumed.114.142729. Disponível em: <http://jnm.snmjournals.org/cgi/doi/10.2967/jnumed.114.142729>.

LEISCHIK, R., DWORRAK, B., SANCHIS-GOMAR, F., *et al.* "Echocardiographic assessment of myocardial ischemia", **Annals of Translational Medicine**, v. 4, n. 13, p. 259–259, jul. 2016. DOI: fpr. Disponível em: <http://atm.amegroups.com/article/view/10987/11532>.

LITJENS, G., KOOI, T., BEJNORDI, B. E., *et al.* **A survey on deep learning in medical image analysis. Medical Image Analysis**. [S.l: s.n.], 2017

LUCAS, BRUCE D. AND KANADE, T. "An Iterative Image Registration Technique with an Application to Stereo Vision". 1981. **Anais [...]** Vancouver, BC, Canada, [s.n.], 1981.

MARINO, M., VERONESI, F., TARRONI, G., *et al.* "Fully automated assessment of left ventricular volumes, function and mass from cardiac MRI". 2014. **Anais [...]** [S.l: s.n.], 2014.

MOORE, C. C., LUGO-OLIVIERI, C. H., MCVEIGH, E. R., *et al.* "Three-dimensional Systolic Strain Patterns in the Normal Human Left Ventricle: Characterization with Tagged MR Imaging", **Radiology**, v. 214, n. 2, p. 453–466, fev. 2000. DOI: 10.1148/radiology.214.2.r00fe17453. Disponível em: <http://pubs.rsna.org/doi/10.1148/radiology.214.2.r00fe17453>.

MORALES, M. A., IZQUIERDO-GARCIA, D., AGANJ, I., *et al.* "Implementation and Validation of a Three-dimensional Cardiac Motion Estimation Network", **Radiology**:

**Artificial Intelligence**, v. 1, n. 4, p. e180080, jul. 2019. DOI: 10.1148/ryai.2019180080.

Disponível em: <http://pubs.rsna.org/doi/10.1148/ryai.2019180080>.

MORALES, M. A., VAN DEN BOOMEN, M., NGUYEN, C., *et al.* "DeepStrain: A Deep Learning Workflow for the Automated Characterization of Cardiac Mechanics",

**Frontiers in Cardiovascular Medicine**, v. 8, n. September, p. 1–16, 3 set. 2021. DOI: 10.3389/fcvm.2021.730316. Disponível em:

<https://www.frontiersin.org/articles/10.3389/fcvm.2021.730316/full>.

MORENO, R. A., DE SÁ REBELO, M. F. S., CARVALHO, T., *et al.* "A combined deep-learning approach to fully automatic left ventricle segmentation in cardiac magnetic resonance imaging". 15 mar. 2019. **Anais [...]** [S.l.], SPIE, 15 mar. 2019. p. 68. DOI:

10.1117/12.2512895. Disponível em: <https://www.spiedigitallibrary.org/conference-proceedings-of-spie/10953/2512895/A-combined-deep-learning-approach-to-fully-automatic-left-ventricle/10.1117/12.2512895.full>.

ØSTVIK, A., SMISTAD, E., ESPELAND, T., *et al.*, "Automatic Myocardial Strain Imaging in Echocardiography Using Deep Learning". [S.l: s.n.], 2018. p. 309–316. DOI:

10.1007/978-3-030-00889-5\_35. Disponível em: [http://link.springer.com/10.1007/978-3-030-00889-5\\_35](http://link.springer.com/10.1007/978-3-030-00889-5_35).

PATEL, A. R., KRAMER, C. M. "Role of Cardiac Magnetic Resonance in the Diagnosis and Prognosis of Nonischemic Cardiomyopathy", **JACC: Cardiovascular Imaging**, v.

10, n. 10, p. 1180–1193, out. 2017. DOI: 10.1016/j.jcmg.2017.08.005. Disponível em: <https://linkinghub.elsevier.com/retrieve/pii/S1936878X17307763>.

PEDRIZZETTI, G., CLAUS, P., KILNER, P. J., *et al.* "Principles of cardiovascular magnetic resonance feature tracking and echocardiographic speckle tracking for informed clinical use", **Journal of Cardiovascular Magnetic Resonance**, v. 18, n. 1, p. 1–12, 26

dez. 2016. DOI: 10.1186/s12968-016-0269-7. Disponível em: <http://jcmr-online.biomedcentral.com/articles/10.1186/s12968-016-0269-7>.

PENSO, M., MOCCIA, S., SCAFURI, S., *et al.* "Automated left and right ventricular chamber segmentation in cardiac magnetic resonance images using dense fully convolutional neural network", **Computer Methods and Programs in Biomedicine**, v. 204, p. 106059, jun. 2021. DOI: 10.1016/j.cmpb.2021.106059. Disponível em: <https://linkinghub.elsevier.com/retrieve/pii/S0169260721001346>.

PETERSEN, S. E., MATTHEWS, P. M., FRANCIS, J. M., *et al.* "UK Biobank's cardiovascular magnetic resonance protocol", **Journal of Cardiovascular Magnetic Resonance**, v. 18, n. 1, p. 8, 1 dez. 2015. DOI: 10.1186/s12968-016-0227-4. Disponível em: <http://jcmr-online.com/content/18/1/8>.

PETITJEAN, C., DACHER, J.-N. "A review of segmentation methods in short axis cardiac MR images", **Medical Image Analysis**, v. 15, n. 2, p. 169–184, abr. 2011. DOI: 10.1016/j.media.2010.12.004. Disponível em: <https://linkinghub.elsevier.com/retrieve/pii/S1361841510001349>.

PIZER, S. M., AMBURN, E. P., AUSTIN, J. D., *et al.* "Adaptive histogram equalization and its variations", **Computer Vision, Graphics, and Image Processing**, v. 39, n. 3, p. 355–368, set. 1987. DOI: 10.1016/S0734-189X(87)80186-X. Disponível em: <https://linkinghub.elsevier.com/retrieve/pii/S0734189X8780186X>.

QIN, C., BAI, W., SCHLEMPER, J., *et al.*, "Joint Learning of Motion Estimation and Segmentation for Cardiac MR Image Sequences". **Lecture Notes in Computer Science (including subseries Lecture Notes in Artificial Intelligence and Lecture Notes in Bioinformatics)**, [S.l: s.n.], 2018. v. 11071 LNCS. p. 472–480. DOI: 10.1007/978-3-030-00934-2\_53. Disponível em: [http://link.springer.com/10.1007/978-3-030-00934-2\\_53](http://link.springer.com/10.1007/978-3-030-00934-2_53).

RADAU P., LU Y., CONNELLY K., PAUL G., DICK A.J., W. G. A. "Evaluation Framework for Algorithms Segmenting Short Axis Cardiac MRI", **MIDAS Journal**, 2009. Disponível em: <http://insight-journal.org/search/?search=authors:Paul>.

RANJAN, A., BLACK, M. J. "Optical Flow Estimation Using a Spatial Pyramid Network". jul. 2017. **Anais** [...] [S.l.], IEEE, jul. 2017. p. 2720–2729. DOI: 10.1109/CVPR.2017.291. Disponível em: <http://ieeexplore.ieee.org/document/8099774/>.

REN, Z., YAN, J., NI, B., *et al.* "Unsupervised deep learning for optical flow estimation", **31st AAAI Conference on Artificial Intelligence, AAAI 2017**, n. Hollingworth 2004, p. 1495–1501, 2017. .

RIBEIRO, M. A. O., NUNES, F. L. S. "Left ventricle segmentation combining deep learning and deformable models with anatomical constraints", **Journal of Biomedical Informatics**, v. 142, p. 104366, jun. 2023. DOI: 10.1016/j.jbi.2023.104366. Disponível em: <https://linkinghub.elsevier.com/retrieve/pii/S1532046423000874>.

RONNEBERGER, O., FISCHER, P., BROX, T., "U-Net: Convolutional Networks for Biomedical Image Segmentation". **MICCAI2015**, [S.l.: s.n.], 2015. p. 234–241. DOI: 10.1007/978-3-319-24574-4\_28. Disponível em: [http://link.springer.com/10.1007/978-3-319-24574-4\\_28](http://link.springer.com/10.1007/978-3-319-24574-4_28).

RUSSELL, S., NORVIG, P. **Artificial Intelligence A Modern Approach**. Englewood Cliffs, New Jersey, Prentice Hall, 1995.

SCATTEIA, A., BARITUSSIO, A., BUCCIARELLI-DUCCI, C. "Strain imaging using cardiac magnetic resonance", **Heart Failure Reviews**, v. 22, n. 4, p. 465–476, 15 jul. 2017. DOI: 10.1007/s10741-017-9621-8. Disponível em: <http://link.springer.com/10.1007/s10741-017-9621-8>.

SEGARS, W. P., STURGEON, G., MENDONCA, S., *et al.* "4D XCAT phantom for

multimodality imaging research", **Medical Physics**, v. 37, n. 9, p. 4902–4915, 24 ago. 2010. DOI: 10.1118/1.3480985. Disponível em: <http://doi.wiley.com/10.1118/1.3480985>.

SIMPSON, R. M., KEEGAN, J., FIRMIN, D. N. "MR assessment of regional myocardial mechanics", **Journal of Magnetic Resonance Imaging**, v. 37, n. 3, p. 576–599, mar. 2013. DOI: 10.1002/jmri.23756. Disponível em: <https://onlinelibrary.wiley.com/doi/10.1002/jmri.23756>.

SUEVER, J. D., WEHNER, G. J., JING, L., *et al.* "Right Ventricular Strain, Torsion, and Dyssynchrony in Healthy Subjects Using 3D Spiral Cine DENSE Magnetic Resonance Imaging", **IEEE Transactions on Medical Imaging**, v. 36, n. 5, p. 1076–1085, maio 2017. DOI: 10.1109/TMI.2016.2646321. Disponível em: <http://ieeexplore.ieee.org/document/7801918/>.

SUINESIAPUTRA, A., COWAN, B. R., AL-AGAMY, A. O., *et al.* "A collaborative resource to build consensus for automated left ventricular segmentation of cardiac MR images", **Medical Image Analysis**, v. 18, n. 1, p. 50–62, jan. 2014. DOI: 10.1016/j.media.2013.09.001. Disponível em: <https://linkinghub.elsevier.com/retrieve/pii/S1361841513001217>.

SUN, D., YANG, X., LIU, M.-Y., *et al.* "PWC-Net: CNNs for Optical Flow Using Pyramid, Warping, and Cost Volume". 7 jun. 2018. **Anais [...] [S.l.]**, IEEE, 7 jun. 2018. p. 8934–8943. DOI: 10.1109/CVPR.2018.00931. Disponível em: <https://ieeexplore.ieee.org/document/8579029/>.

TRAN, P. V. "A Fully Convolutional Neural Network for Cardiac Segmentation in Short-Axis MRI", p. 1–21, 2 abr. 2016. Disponível em: <http://arxiv.org/abs/1604.00494>.

TU, Z., XIE, W., ZHANG, D., *et al.* "A survey of variational and CNN-based optical flow



techniques", **Signal Processing: Image Communication**, v. 72, n. October 2018, p. 9–24, mar. 2019. DOI: 10.1016/j.image.2018.12.002. Disponível em: <https://doi.org/10.1016/j.image.2018.12.002>.

VO, H. Q., MARWICK, T. H., NEGISHI, K. "MRI-Derived Myocardial Strain Measures in Normal Subjects", **JACC: Cardiovascular Imaging**, v. 11, n. 2, p. 196–205, fev. 2018. DOI: 10.1016/j.jcmg.2016.12.025. Disponível em: <https://linkinghub.elsevier.com/retrieve/pii/S1936878X1730253X>.

VOIGT, J.-U., CVIJIC, M. "2- and 3-Dimensional Myocardial Strain in Cardiac Health and Disease", **JACC: Cardiovascular Imaging**, v. 12, n. 9, p. 1849–1863, set. 2019. DOI: 10.1016/j.jcmg.2019.01.044. Disponível em: <https://linkinghub.elsevier.com/retrieve/pii/S1936878X19306096>.

WAPCAPLET, Y. **Diagram\_of\_the\_human\_heart.svg**. 2003. Wikimedia Commons. Disponível em: [https://commons.wikimedia.org/wiki/File:Diagram\\_of\\_the\\_human\\_heart.svg](https://commons.wikimedia.org/wiki/File:Diagram_of_the_human_heart.svg).

WEBSTER, J. "Medical instrumentation: application and design, Fourth edition.", **John Wiley and Sons, Inc. USA**, 2010. .

WISSMANN, L., SANTELLI, C., SEGARS, W. P., *et al.* "MRXCAT: Realistic numerical phantoms for cardiovascular magnetic resonance", **Journal of Cardiovascular Magnetic Resonance**, v. 16, n. 1, p. 63, 20 dez. 2014. DOI: 10.1186/s12968-014-0063-3. Disponível em: <http://jcmr-online.biomedcentral.com/articles/10.1186/s12968-014-0063-3>.

WORLD HEALTH ORGANIZATION. **Cardiovascular diseases (CVDs)**. 2021. Disponível em: [https://www.who.int/news-room/fact-sheets/detail/cardiovascular-diseases-\(cvds\)](https://www.who.int/news-room/fact-sheets/detail/cardiovascular-diseases-(cvds)). Acesso em: 18 fev. 2023.

XU, C., XU, L., GAO, Z., *et al.* "Direct delineation of myocardial infarction without contrast agents using a joint motion feature learning architecture", **Medical Image Analysis**, v. 50, n. 2018, p. 82–94, 2018. DOI: 10.1016/j.media.2018.09.001. Disponível em: <https://doi.org/10.1016/j.media.2018.09.001>.

YU, J. J., HARLEY, A. W., DERPANIS, K. G., "Back to Basics: Unsupervised Learning of Optical Flow via Brightness Constancy and Motion Smoothness". **Lecture Notes in Computer Science (including subseries Lecture Notes in Artificial Intelligence and Lecture Notes in Bioinformatics)**, [S.l: s.n.], 2016. p. 3–10. DOI: 10.1007/978-3-319-49409-8\_1. Disponível em: [http://link.springer.com/10.1007/978-3-319-49409-8\\_1](http://link.springer.com/10.1007/978-3-319-49409-8_1).

ZHANG, K. W., FRENCH, B., MAY KHAN, A., *et al.* "Strain improves risk prediction beyond ejection fraction in chronic systolic heart failure.", **Journal of the American Heart Association**, v. 3, n. 1, p. 1–10, 2014. DOI: 10.1161/JAHA.113.000550. .

ZHENG, Q., DELINGETTE, H., AYACHE, N. "Explainable cardiac pathology classification on cine MRI with motion characterization by semi-supervised learning of apparent flow", **Medical Image Analysis**, v. 56, p. 80–95, 2019. DOI: 10.1016/j.media.2019.06.001. Disponível em: <https://doi.org/10.1016/j.media.2019.06.001>.